Title: **A human-ACE2 knock-in mouse model for SARS-CoV-2 infection recapitulates respiratory disorders but avoids neurological disease associated with the transgenic K18-hACE2 model.**

Running title: B.1 SARS-CoV-2 infection of a new hACE-2 Knock-in mice

Anna Pons-Grífols[1], Ferran Tarrés-Freixas[1,2,3,4], Mònica Pérez[2,3], Eva Riveira-Muñoz[1], Dàlia Raïch-Regué[1], Daniel Pérez-Zsolt[1], Jordana Muñoz-Basagoiti[1], Barbara Tondelli[5], Edwards Pradenas[1], Nuria Izquierdo-Useros[1,6,7,], Sara Capdevila[8], Júlia Vergara-Alert[2,3], Victor Urrea[1], Jorge Carrillo[1,6,7], Ester Ballana[1,6], Stephen Forrow[5], Bonaventura Clotet[1,4], Joaquim Segalés[2,9], Benjamin Trinité[1,#], Julià Blanco[1,4,6,7,#].

[1]IrsiCaixa, Can Ruti Campus, Badalona, Spain.
[2]Unitat mixta d'investigació IRTA-UAB en Sanitat Animal, Centre de Recerca en Sanitat Animal (CReSA), Campus de la Universitat Autònoma de Barcelona (UAB), Bellaterra, Spain.
[3]IRTA, Programa de Sanitat Animal, Centre de Recerca en Sanitat Animal (CReSA), Campus de la Universitat Autònoma de Barcelona (UAB), Bellaterra, Spain.
[4]University of Vic-Central University of Catalonia (UVic-UCC), Vic, Spain.
[5]Mouse Mutant Core Facility (PBA2B2), Institute for Research in Biomedicine (IRB), Parc Científic de Barcelona, Barcelona, Spain.
[6]Germans Trias i Pujol Research Institute (IGTP), Badalona, Spain.
[7]CIBER Infectious Diseases (CIBERINFEC), Carlos III Health Institute, Madrid, Spain.
[8]Comparative Medicine and Bioimage Centre of Catalonia (CMCiB), Germans Trias i Pujol Research Institute (IGTP), Badalona, Spain.
[9]Departament de Sanitat i Anatomia Animals, Facultat de Veterinària, Universitat Autònoma de Barcelona (UAB), Campus de la UAB, Bellaterra, Spain.

 # Corresponding authors

Benjamin Trinité: btrinite@irsicaixa.es

Julià Blanco: jblanco@irsicaixa.es

JS, BT and JB are co-senior authors

Abstract Word count: 242
Text word count: 5984

Abstract

Animal models have been instrumental in elucidating the pathogenesis of SARS-CoV-2 infection and testing COVID-19 vaccines and therapeutics. Wild-type (WT) mice are not susceptible to many SARS-CoV-2 variants, therefore transgenic K18-hACE2 mice have emerged as a standard model system. However, this model is characterized by severe disease, particularly associated with neuroinfection, which leads to early humane endpoint euthanasia. Here, we established a novel knock-in (KI) mouse model by inserting the original K18-hACE2 transgene into the collagen COL1A1 locus using a recombinase mediated cassette exchange (RMCE) system. Once the Col1a1-K18-hACE2 mouse colony was established, animals were challenged with a B.1 SARS-CoV-2 (D614G) isolate and were monitored for up to 14 days. Col1a1-K18-hACE2 mice exhibited an initial weight loss similar to the K18-hACE2 transgenic model but did not develop evident neurologic clinical signs. The majority of Col1a1-K18-hACE2 mice did not reach the preestablished humane endpoint, showing progressive weight gain after 9 days post-infection (dpi). Importantly, despite this apparent milder pathogenicity of the virus in this mouse model compared to the K18-hACE2 transgenic model, high levels of viral RNA were detected in lungs, oropharyngeal swab, and nasal turbinate. Remaining lesions and inflammation in lungs were still observed after 14 dpi. In contrast, although low level viral RNA could be detected in a minority of Col1a1-K18-hACE2 animals, no brain lesions were observed at any timepoint. Overall, Col1a1-K18-hACE2 mice constitute a new model for investigating SARS-CoV-2 pathogenesis and treatments, with potential implications for studying long-term COVID-19 sequelae.

Importance

K18-hACE2 mice express high levels of the human protein ACE2, the receptor for SARS-CoV-2, and can therefore be infected by this virus. These animals have been crucial to understand viral pathogenesis and to test COVID-19 vaccines and antiviral drugs. However, K18-hACE2 often die after infection with initial SARS-CoV-2 variants likely due to a massive brain infection that does not occur in humans. Here, we used a technology known as knock-in that allows for the targeted insertion of a gene into a mouse and we have generated a new hACE2-mouse. We have characterized this new animal model demonstrating that the virus replicates in the respiratory tract, damaging lung tissue and causing inflammation. In contrast to K18-hACE2 mice, only limited or no brain infection could be detected, and most animals recovered from infection with remaining lung lesions. This new model could be instrumental for the study of specific disease aspects such as post-COVID condition, sequelae, and susceptibility to reinfection.

Keywords: animal model, lung inflammation, lung damage, neuroinvasion, post covid condition.

75 **Introduction**

76 Severe Acute Respiratory Syndrome Coronavirus 2 (SARS-CoV-2) is the etiologic agent of the
77 coronavirus disease 2019 (COVID-19). The COVID-19 pandemic fueled an unprecedented
78 collaborative research effort to develop therapeutics and vaccines. Animal models that
79 recapitulate key clinical and pathological features of COVID-19 have played a pivotal role in
80 testing novel vaccines, antivirals and other treatments (1).

81 The spike glycoprotein of SARS-CoV-2 uses the angiotensin-converting enzyme 2 (ACE2) as
82 receptor to enter and infect host cells (2). ACE2 is expressed on the surface of cells of
83 different organs such as lungs, intestines, kidneys, and heart. However, the spike
84 glycoprotein from ancestral SARS-CoV-2 strains does not efficiently bind to mouse ACE2
85 (mACE2), rendering wild-type (WT) mice refractory to infection. Therefore, several
86 strategies were used to develop mouse models susceptible to infection. These strategies
87 include viral adaptation (3) or the introduction of the human ACE2 (hACE2) receptor via viral
88 vectors and transgenic approaches (4–8).

89 Both K18-hACE2 transgenic mice and Golden Syrian hamsters (GSH) became reference
90 animal models for investigating SARS-CoV-2 pathogenesis in vivo. They mainly differ in
91 pathogenesis: GSH, which are naturally susceptible to SARS-CoV2 infection, recapitulate a
92 milder disease phenotype (1). The K18-hACE2 mouse model was originally developed for
93 the study of SARS-CoV, which also targets hACE2. It was created by random insertion of
94 multiple copies of the *hACE2* gene under the control of the human cytokeratin 18 gene
95 promoter (*KRT18* or K18). This promoter allows for high-level expression and is specific to
96 epithelial cells, including those in the airways (9, 10). This approach allows the infection of

97 mice by SARS-CoV-2, while maintaining the activity of the mACE2 receptor. Infection of K18-
98 hACE2 mice with pre-Omicron variants of SARS-CoV-2 results in progressive weight-loss and
99 strong clinical signs by 3-5 days post-infection (dpi), a severity which often requires
100 euthanasia by 5-7 dpi. The lethality in this model is dose- and SARS-CoV-2 variant-
101 dependent (10, 11), and has been associated with neuroinvasion and extensive brain
102 infection (9, 12–14). Neuroinvasion in K18-hACE2 transgenic mice has been linked to the
103 aleatory gene insertion and the high number of inserted gene copies, around 8 in the
104 commercial *B6.Cg-Tg(K18-ACE2)2Prlmn/J-K18-hACE2 mouse* (10), leading to altered
105 expression levels and tissue distribution of the receptor (15). Specifically, a higher number
106 of gene copies correlates with a worse disease prognosis and encephalitis in this model,
107 following SARS-CoV infection (16). These neurological lesions leading to death are not
108 consistent with the pathology of COVID-19 in humans, in which infection of the central
109 nervous system can be detected post-mortem in severe COVID-19 cases, although to a
110 lower extent and unrelated to the severity of brain lesions (17, 18). Therefore, new mouse
111 models that better recapitulate the human disease, without lethal viral neuroinvasion,
112 could complement other existing animal models (hamster or NHP) (1).

113 Knock-in (KI) models are characterized by the targeted insertion of a defined gene copy
114 number in a specific locus, therefore allowing for a more accurate and predictable
115 expression of the transgene. In this work, we used a recombinase-based approach to insert
116 the original K18-hACE2 transgene into the collagen type I alpha chain (COL1A1) locus to
117 generate a Col1a1-K18-hACE2 KI mouse. To characterize this new model, mice were
118 challenged with SARS-CoV-2 B.1 (D614G) isolate and pathogenicity was compared with the

119 well-characterized K18-hACE2 transgenic mice. After viral challenge of Col1a1-K18-hACE2
120 mice, we confirmed viral replication and histological lesions in the lungs, but minimal viral
121 neuroinvasion.

122

123 **Results**

124 **Assessment of hACE2 expression in the Col1a1-K18-hACE2 mice**

125 We generated a new hACE2 KI mouse model through addition of the original K18-hACE2
126 transgene, kindly supplied by Paul McCray (9) at the COL1A1 locus using a recombinase
127 mediated system (**Figure 1A**) (19). Traditional transgenic techniques rely on the random
128 genomic insertion of an unpredictable number of transgene copies. This frequently results
129 in a highly variable level and pattern of transgene expression, due to cis acting regulatory
130 elements at the site of insertion. A single copy of a transgene, inserted into the well
131 characterised Col1A1 locus, is expected to result in a more predictable level and pattern of
132 expression of the transgene sequence. To confirm the correct expression of the transgene
133 in this KI model, we initially quantified *hACE2* transcripts relative to the house-keeping gene
134 GAPDH by RT-qPCR in RNA samples extracted from twelve different tissues. Expression of
135 the hACE2 mRNA in K18-hACE2 mice was similar among most tested tissues except in
136 muscle and heart, which showed lower values (**Figure 1B).** In contrast, hACE2 mRNA
137 expression in Col1a1-K18-hACE2 mice was more heterogenous, with the lowest expression
138 observed in the brain and liver. When comparing the relative expression of hACE2 mRNA
139 between both models, we observed higher expression in the pancreas, lymph nodes and
140 muscle of Col1a1-K18-hACE2 mice. Conversely, in the kidney, brain and liver, hACE2 mRNA
141 expression was higher in the K18-hACE2 mouse model. Minor differences were observed in
142 the rest of the analyzed tissues (**Figure 1C**). To complement mRNA expression data, protein
143 expression was assessed by Wester-blot (WB) in 6 different tissues using a monoclonal
144 antibody specific for hACE2 (20) and a polyclonal antibody recognizing both hACE2 and

145 mACE2. GAPDH was used as control, and tissues from Col1a1-K18-hACE2, K18-hACE2 and
146 WT mice were analyzed. Data showed undetectable protein expression in muscle, and
147 higher hACE2 expression in lung, pancreas and spleen of Col1a1-K18-hACE2 mice compared
148 to K18-hACE2 animals **(Figure 1D)**. Conversely, as observed by RT-qPCR, a higher hACE2
149 expression was detected in K18-hACE2 brain and liver compared to Col1a1-K18-hACE2
150 samples **(Figure 1D)**.

151 **Survival of Col1a1-K18-hACE2 mice following SARS-CoV-2 B.1 infection**.

152 Col1a1-K18-hACE2 mice (n=27) and K18-hACE2 mice (n=4) were challenged intranasally
153 with a SARS-CoV-2 B.1 (D614G) isolate. Uninfected KI animals, used as a control, received
154 an intranasal dose of PBS (n=5). Animal weight and clinical signs were monitored daily for
155 14 days after infection. The endpoints to collect samples were set at 3-, 7-, and 14-days
156 post-infection (dpi, n=8 Col1a1-K18-hACE2 mice per endpoint) or upon fulfilment of
157 humane endpoint criteria (**Figure 2A**).

158 Consistent with previous studies in transgenic animals with the B.1 SARS-CoV-2 variant,
159 weight-loss could be observed in both animal models starting around 3 dpi (**Figure 2B**) (13).
160 In K18-hACE2 transgenic animals, the decrease in weight was associated with the
161 progressive appearance of severe clinical signs: decrease in mobility, dyspnea, and
162 neurological effects **(Supplementary Table 1),** fulfilling the humane endpoint criteria and
163 leading to euthanasia of all K18-hACE animals by 6 or 7dpi (**Figure 2C**). In contrast, while
164 Col1a1-K18-hACE2 mice underwent weight loss, they did not show severe clinical signs
165 apart from a slight decrease in activity. Three Col1a1-K18-hACE2 animals had to be

166 euthanized (exitus) exclusively due to their weight loss exceeding the 20% limit (humane
167 endpoint) at 8, 9 and 10 dpi. Convalescent animals started to regain weight after 9 dpi,
168 reaching 90% of their initial weight by 14 dpi (**Figure 2B/C**). These results indicate that B.1
169 SARS-CoV-2 infection is significantly less pathogenic in Col1a1-K18-hACE2 mice than in K18-
170 hACE2 transgenic mice (**Figure 2C**).

171 **SARS-CoV-2 B.1 replicates in the respiratory tract of Col1a1-K18-hACE2 KI mice**.

172 To fully characterize the kinetics of viral replication in the respiratory tract, samples from
173 oropharyngeal swab, lung, and nasal turbinate were collected at 3, 7, and 14 dpi or at the
174 humane endpoint (exitus) in all Col1a1-K18-hACE2 mice (n=32). Samples from K18-hACE2
175 transgenic mice obtained at euthanasia (6 and 7 dpi) were used as reference (n=4). Viral
176 RNA analysis in oropharyngeal swab, lung, and nasal turbinate revealed widespread
177 infection in both K18-hACE2 and Col1a1-K18-hACE2 mice in all mentioned tissues across
178 two independent experiments (**Figure 3A**). VL in the nasal turbinate were similar in both
179 animal models, with some viral RNA was still detected at 14 dpi in Col1a1-K18-hACE2 mice.
180 RNA levels in oropharyngeal swabs and lung peaked at 3 dpi in Col1a1-K18-hACE2 mice and
181 tended to decay overtime up to 14 dpi. To further confirm viral clearance, titration of
182 replication-competent virus was performed in lung samples. Similar to the VL kinetics, viral
183 titers peaked at 3 dpi, followed by a quick and significant decrease (**Figure 3B,** 3 dpi vs 7 dpi:
184 p = 0.00178), concomitant with the elicitation of neutralizing antibodies **(Supplementary**
185 **Figure 1).** Col1a1-K18-hACE2 animals euthanized at the humane endpoint at 8-10 dpi still
186 displayed high viral RNA in lungs, which could explain their more pronounced weight-loss
187 and early fulfilment of endpoint criteria. However, high titers of neutralizing antibodies in

188 these animals probably prevented the recovery of infectious viruses **(Figure 3B and**
189 **Supplementary Fig 1).**

190 To characterize histopathological changes, formalin-fixed lung samples from both animal
191 models were analyzed by histology and immunohistochemistry (IHC) to score the presence
192 and extension of lesions and SARS-CoV-2 nucleoprotein antigen (NP), respectively.
193 Histological lesions were semi-quantified as none, mild, moderate, or severe (score 0-3),
194 and the detection of viral antigen as lack, low, moderate, or high (score 0-3). In Col1a1-K18-
195 hACE2 KI mice, histopathological analysis showed development of bronchointerstitial
196 pneumonia characterized by multifocal increased thickness of interalveolar wall, presence
197 of macrophage-like cells into alveoli surrounding bronchi and bronchiole, and hyperplasia
198 of type II pneumocytes. These lesions evolved from mild and multifocal by 3 dpi to moderate
199 in most of the animals by 14 dpi, also with increasing lymphoplasmacytic infiltration until
200 the end of the study. The extension of hyperplasia of type II pneumocytes was barely
201 detected at 3 dpi, mild by 7 dpi and moderate by 14 dpi. Therefore, an increase in lung lesion
202 average was observed over time **(Figure 3C and D).** Animals reaching humane endpoint
203 displayed areas of severe bronchointerstitial pneumonia (**Supplementary Figure 2**). IHC
204 detection of SARS-CoV-2 NP in the lungs of Col1a1-K18-hACE2 KI mice was consistent with
205 the VL analyses, showing the highest score early upon infection (3 dpi). Antigen detection
206 decreased with time showing apparent clearance by 14 dpi **(Figure 3C and D).** However,
207 animals reaching humane endpoint at 8,9 and 10 dpi showed mild to moderate SARS-CoV-
208 2 antigen staining mainly located in bronchiolar epithelium from different bronchiole
209 (**Supplementary Figure 2**).

210 To assess infection-driven inflammation, we analyzed the levels of IL-6 and IFNγ cytokines,
211 involved in inflammation and immune activation; and IP-10, MCP-1 and MIP-1β
212 chemokines, primarily involved in the recruitment of immune cells. Cytokine and chemokine
213 levels were measured by Luminex in lung samples from both animal models at the indicated
214 timepoints. While all markers were increased in infected animals, compared to uninfected
215 controls, IP-10 and IL-6 peaked at 3 dpi and significantly decreased by 14 dpi in Col1a1-K18-
216 hACE2 KI mice (**Figure 4**). In contrast, IFNγ, MCP-1, and MIP1β peaked at 7 dpi and decayed
217 afterwards, although no statistical differences were observed among the analyzed
218 timepoints. Overall, levels of inflammatory mediators at 7 dpi in Col1a1-K18-hACE2 KI mice
219 were comparable to K18-hACE2 transgenic mice at the time of euthanasia (6 and 7 dpi).
220 Residual levels of IFNγ and MIP1β were observed at 14dpi in some Col1a1-K18-hACE2 mice,
221 probably associated with the remaining tissue lesions at this time point, since no viral
222 antigen could be detected **(Figure 4. C-D).**

223 **SARS-CoV-2 B.1 replication in other tissues**

224 To explore the extent of viral infection in both animal models, viral loads (VL, cell-free viral
225 RNA) were quantified in a large set of samples (brain, muscle, intestine, liver, kidney,
226 pancreas, salivary glands, lymph nodes and spleen) collected from a subset of animals
227 (n=20). In both models, VL were mostly undetected in most tissues except for low levels
228 found in the heart and salivary glands (**Figure 5**). The analysis of brain samples showed high
229 VL exclusively in K18-hACE2 transgenic animals. However, the initial screening of brain
230 tissue from Col1a1-K18-hACE2 mice showed low but detectable VL in one animal at 3 dpi

231 and two animals at 7 dpi. In sharp contrast, euthanized animals, which showed the highest
232 weight loss and lung VL, lacked detectable VL in the brain (**Figure 5**).

233

234 **Col1a1-K18-hACE2 KI mice do not develop massive brain infection.**

235 To further investigate the level of viral infection in the brain (**Figure 5**), we performed a
236 longitudinal virological and histological analysis of brain samples in all animals (n=32).
237 Considering the full set of data, VL was detected at low levels in 3 of 8 Col1a1-K18-hACE2
238 mice at 3dpi and 2 out of 8 Col1a1-K18-hACE2 KI mice at 7 dpi. No VL was found in the
239 additional animal that reached the humane endpoint. In contrast, all K18-hACE2 brain
240 samples showed significantly higher VL at euthanasia (6-7dpi) (**Figure 6A**). However, no
241 infective virus could be found in any Col1a1-K18-hACE2 mice at any timepoint by viral
242 titration, while all K18-hACE2 presented high viral titers at 6-7dpi (**Figure 6B**).

243 For histological analysis, formalin-fixed brain samples were scored in a blinded fashion as
244 described above. Histopathological analysis of the brain in the Col1a1-K18-hACE2 model
245 showed no lesions at any of the analyzed timepoints nor those animals that required
246 humane endpoint (**Supplementary Figure 2**). In contrast, brain samples from K18-hACE2
247 infected animals showed lesion scores between 1 and 2 **(Figure 6C,Left).** Furthermore, no
248 detection of SARS-CoV-2 NP antigen in the brain of Col1a1-K18-hACE2 mice was observed
249 by IHC at any timepoint **(Figure 6C)** or at the humane endpoint **(Supplementary Figure 1);**
250 while K18-hACE2 mice showed a high density of antigen diffused throughout the tissue
251 (score 3) at euthanasia **(Figure 6C, Right).** Brain changes in the transgenic model were

252 consistent with the widely reported pathology induced by initial SARS-CoV-2 variants (12,

253 14, 21) and were observed alongside the detection of viral antigen in the brain (**Figure 6D**).

254

255 **Discussion**

256 In this study, we characterized a novel hACE2 KI murine model by evaluating the course of
257 infection with the B.1 D614G SARS-CoV-2 variant with a direct comparison to the well-
258 described K18-hACE2 transgenic mouse model, in which this variant is known to be highly
259 pathogenic. The most relevant findings included the susceptibility of the KI model to SARS-
260 CoV-2 infection and the reduced lethality imputed to the reduced viral replication and
261 lesions in the brain.

262 The development of this KI model was started at the beginning of the COVID-19 pandemic
263 as an alternative to the K18-hACE2 transgenic mouse model. Even though the transgenic
264 model had already been established and used in previous SARS-CoV studies (9), the
265 availability of these animals was limited at first, as colonies needed to be restarted from
266 cryopreserved embryos. In this context, several laboratories developed new hACE2 murine
267 models for SARS-CoV-2 infection. Expression of the hACE2 transgene was achieved through
268 various methods, including directed insertion using CRISPR/Cas9 technology (20) using
269 different promoters such as Hepatocyte nuclear factor-3/forkhead homologue 4 (Hfh4)
270 promoter (5) or the mouse ACE2 promoter (6), and by infecting mice with replication-
271 defective adenovirus encoding hACE2 (3). In this work, we followed a different strategy
272 wherein a single copy of the transgene was inserted into the COL1A1 locus, but under the
273 K18 promoter as the original transgenic K18-hACE2 model. The selection of this locus was
274 based on its known ability to provide reliable and ubiquitous expression of inserted
275 sequences (19). Additionally, RMCE allowed the insertion of a single transgene copy which
276 should better mimic physiological expression, potentially impacting lethality through

277 reduction of the ectopic expression and modification of tissue distribution of the hACE2
278 receptor. A recent study identifying a correlation between lower hACE2 copy number and
279 reduced pathogenicity further supports our initial hypothesis (22).

280 When compared with K18-hACE2 transgenic mice, B.1 infection of the new Col1a1-K18-
281 hACE2 KI mouse model resulted in much less severe clinical signs with better responsiveness
282 to stimuli, better physical appearance and no neurological signs. These observations were
283 consistent with a lower viral replication in brain of Col1a1-K18-hACE2 KI mice, as
284 summarized in **Supplementary Figure 3**. Focusing on the respiratory tract, viral replication
285 was observed in both models, although VL and antigen detection were in general lower at
286 7 dpi in Col1a1-K18-hACE2 KI mice. In contrast, lung tissue lesions and inflammation were
287 fully comparable in both models at this timepoint (**Supplementary Figure 3)**.

288 To explain the different pathogenicity between each model, hACE2 expression was analyzed
289 in different tissues. At mRNA level, expression in the lungs and nasal turbinates was
290 comparable or higher in Col1a1-K18 hACE2 mice, while the brain and liver showed lower
291 hACE2 expression, as reported for other transgenic approaches (22, 23). Expression of
292 hACE2 protein showed additional differences; it confirmed lower expression in brain and
293 liver and higher expression in pancreas of Col1A1-K18-hACE2 animals, but revealed higher
294 expression in lung and spleen. In general, brain hACE2 expression in this new KI model
295 seems to be closer to the physiological situation in humans, which showed low expression
296 in the CNS, based on several techniques including transcriptomics and IHC (24). Among the
297 clinical parameters analyzed in Col1a1-K18-hACE2 KI infected mice, we found that initial
298 weight-loss was similar to that of the K18-hACE mice but was not accompanied by the

299 increased severity of clinical signs that characterizes infection in these transgenic mice
300 (neurological signs, lack of responsiveness, and poor general appearance) (13). Consistent
301 with this observation, infection of Col1a1-K18-hACE2 KI mice led to partial recovery in
302 weight by 14 dpi in most animals. Importantly, the survival rate of Col1a1-K18-hACE2 KI
303 mice was over 70%, with three euthanized animals exclusively due to a weight loss of more
304 than 20%, which was one of the humane endpoints in our study. These data are in line with
305 other hACE2 KI mouse models in which substantial viral replication within the upper and
306 lower respiratory tracts with limited spread to extrapulmonary organs has been described
307 (8, 22, 25).

308 Among the tissues analyzed in Col1a1-K18-hACE2 KI infected mice, we found significant
309 replication of SARS CoV-2 in the respiratory tract, mainly in the lungs. Despite viral clearance
310 in Col1a1-K18-hACE2 KI mice which was confirmed by viral titration and IHC, lung lesions
311 were similar between both models by 7dpi and remained after 14 dpi in KI animals
312 recovering from the infection. The impact of viral replication on lung inflammation in
313 Col1a1-K18-hACE2 was confirmed and found to be comparable to the inflammation profile
314 reported in K18-hACE2 transgenic mice (21, 26). Infection of Col1a1-K18-hACE2 KI mice
315 induced high levels of IFNγ, IL-6, IP-10, MCP-1 and MIP-1β cytokines. The longitudinal
316 analysis showed early impact on IL-6 and IP-10 levels (3 dpi) and a clear trend to
317 normalization by 14 dpi, with some residual inflammation remaining. This is consistent with
318 the presence of lesions at this timepoint, and the immune cell infiltration described by 21
319 dpi in K18-hACE2 transgenic mice surviving infection (21).

320 The main difference between the Col1a1-K18-hACE2 KI and the K18-hACE2 transgenic
321 models was found in neuroinvasion. Residual levels of viral RNA but no replication
322 competent virus or viral proteins were detected in the brains of Col1a1-K18-hACE2 KI mice.
323 Furthermore, no detectable brain lesions, such as the multifocal lymphoplasmacytic
324 meningoencephalitis reported in K18-hACE2 transgenic mice (14) were detected by
325 histology, and no SARS-CoV-2 nucleoprotein could be evidenced by IHC. Importantly, the
326 three animals that reached humane endpoints did not present any evidence of brain viral
327 replication but showed enhanced lung infection. Considering that the expression of hACE2
328 is lower in brain and higher in lung in Col1a1-K18-hACE2 compared to K18-hACE2, it seems
329 that the targeted insertion of the hACE2 transgene can be a crucial factor leading to lower
330 levels of brain infection and neurological clinical signs, as well as enhanced respiratory
331 affection in this new model. However, different studies have shown that neuroinvasion is
332 only partially dependent on the expression of hACE2 receptor (12), and that both delivery
333 route and viral dose can play a role in the magnitude of the neuroinvasion (23, 27). In our
334 case, to exclusively analyze the effect of receptor expression, we kept the intranasal
335 administration route and $TCID_{50}$ dose established and characterized in our own and others'
336 studies to ensure comparability of the results (13, 28).

337 Our study is a preliminary characterization of a new animal model and has consequently
338 several limitations. The first limitation was the age of the animals used. The Col1a1-K18-
339 hACE2 mice ranged in age from 5 to 11 months, depending on availability at the time of the
340 study. However, although pathogenicity of SARS-CoV-2 infection has the potential to be
341 higher in older animals, we could not detect significant age differences between euthanized

342 and convalescent animals (mean+/-SD age of 9.1+/-2.0 and 8.0+/-2.1 months, respectively).
343 Second, the expression of hACE2 has been analyzed at both the mRNA and protein levels in
344 bulk tissues, but a further characterization in specific cell types will be necessary to link
345 expression levels with pathology. Moreover, we have focused on the characterization of
346 one viral variant and a single dose. The B.1 variant was selected for its demonstrated
347 severity in K18-hACE2 mice and its inability to use mACE2 as an entry receptor, unlike
348 B.1.351/Beta and Omicron BA1.1 variants (13, 15). While ancestral and earlier variants
349 (B.1.1.7/Alpha, B.1.351/Beta B.1.617.2/Delta) were highly pathogenic in K18-hACE2 mice,
350 Omicron BA.1.1 caused a milder infection with no weight loss nor neuroinvasion, therefore
351 reducing lethality in this model (13). However, more recent Omicron subvariants such as
352 BQ.1.1, BA.5 and XBB.1.5 appear to be regaining pathogenicity in K18-hACE2 mice (29–31).
353 Increased lung infection, pro-inflammatory cytokines, and lung pathology are observed with
354 these variants, with data on neuroinvasion and neurovirulence on the latter (31). Similarly,
355 lower omicron variants has been described in KI mice (25, 32). Nevertheless, for the B.1
356 SARS-CoV-2 variant the Col1a1-K18-hACE2 model shows similarity with GSH in viral
357 dynamics and pathology, with minimal neuroinvasion. This new model, however, has the
358 upside of a wider reagent availability, scarce in GSH (1), and easier animal facility allowance.

359 In summary, several mouse models for the evaluation of antivirals and vaccines have been
360 developed to date, with disease phenotypes ranging from mild to severe COVID-19-like
361 condition. None of these models, however, can fully recapitulate all aspects of the disease
362 as it occurs in humans. The development and further characterization of new animal
363 models, like the Col1a1-K18-hACE2 model, may overcome some of these limitations and

364 provide valuable tools to study certain aspects of COVID-19. Survival of Col1a1-K18-hACE2
365 KI mice after infection with a highly pathogenic variant could provide a model which better
366 mimics human disease progression and thus could be instrumental for the study of specific
367 disease aspects such as the consequences of inflammation (including loss of taste or smell)
368 post-COVID conditions (PCC) or sequelae, long-term effects of drug therapies, and
369 susceptibility to reinfection.

370

371 Materials and methods

372 Creation of the Knock-in Model

373 A new KI mouse model, **B6;129S-Col1a1$^{tm1(K18\text{-}hACE2)Irb}$/Irsi** (Col1a1-K18-hACE2), was created
374 by inserting the original K18-hACE2 transgene into the collagen COL1A1 locus using a
375 recombinase-mediated cassette exchange (RMCE) FLP-FRT system in KH2 cells (19). The
376 actual insertion site lies approximately 0.3 kb downstream of the 3'UTR end of COL1A1. As
377 such, the inserted transgene remains identical to the original designed one (9) and the
378 hACE2 cDNA is under the control of the K18 promoter rather than COL1A1. Specifically, the
379 plasmid PGK-ATG-Frt was digested with EcoRV, and the sequence
380 ATCAGACGTCGCTAGCGGCGCGCCGGTACTAGT was inserted to create a multi-cloning site.

381 The plasmid containing hACE2 under the control of the K18 promoter (K18-hACE2), supplied
382 by Paul McCray, was digested with HpaI and XbaI enzymes. The resulting transgene
383 fragment was isolated and purified, and then cloned into the EcoRV-NheI sites of the
384 modified PGK-ATG-Frt plasmid to generate the targeting vector. The targeting vector was
385 then co-transfected with an Flp expression construct into KH2 cells by electroporation. The
386 cells were then placed under hygromycin selection for 9 days, after which drug resistant
387 colonies were picked, expanded, and screened for the presence of the targeted transgene.
388 Once confirmed, the modified embryonic stem cells were injected into mouse blastocysts.
389 These injected mouse blastocysts were then placed into recipient foster females via embryo
390 transfer techniques.

391 Biosafety Approval and Virus Isolation

392 The execution of SARS-CoV-2 experiments was approved by the biologic biosafety
393 committee of Germans Trias i Pujol Research Institute (IGTP) and performed at the Biosafety
394 Level 3 laboratory (BSL-3) of the Comparative Medicine and Bioimage Centre (CSB-20-015-
395 M8; CMCiB, Badalona, Spain).

396 The B.1 SARS-CoV-2 isolate used in this study was isolated from nasopharyngeal swabs of
397 hospitalized patients in Spain as described elsewhere (33, 34). Briefly, viruses were
398 propagated in Vero E6 cells (CRL-1586; ATCC, Virginia, VA, United States) for two passages
399 and recovered by supernatant collection. The sequence of the SARS-CoV-2 variant tested is
400 deposited at the GISAID Repository with accession IDs EPI_ISL_510689. EPI_ISL_510689 was
401 the first SARS-CoV-2 virus isolated in Catalonia in March 2020 and, compared to the Wuhan/
402 Hu-1/2019 (WH1) strain, this isolate had the S protein mutations D614G, which is associated
403 with the B.1 lineage, and R682L. Viral stocks were titrated on Vero E6 cells to use equivalent
404 TCID50/mL using the Reed-Muench method and sequential 1/10 dilutions of the viral stocks
405 as described previously (34).

406 Animal Procedures and Study Design

407 All animal procedures were approved by the Committee on the Ethics of Animal
408 Experimentation of the IGTP and were authorized by the *Generalitat de Catalunya* (code:
409 11222). All animal experiments followed the principles of animal welfare and the 3Rs. All
410 experiments and sample processing were performed inside the BSL-3 facility. Col1a1-K18-
411 hACE2 hemizygous KI mice were produced and bred at Parc Científic de Barcelona (PCB) by
412 pairing hemizygous males for Tg(K18-ACE2)2Prlmn (or K18-hACE2) with non-carrier

413 C57Bl6/J females. Animals used as control, B6.Cg-Tg(K18-ACE2)2Prlmn/J (or K18-hACE2)
414 hemizygous transgenic mice (034860, Jackson Immunoresearch, West Grove, PA, United
415 States) were bred at CMCiB in the Specific Pathogen Free Area (SPF) by pairing hemizygous
416 K18-hACE2 males with non-carrier C57Bl6/J females. The genotype of the offspring
417 regarding both K18-hACE2 and Col1a1-K18-hACE2 mice was determined by qPCR at the
418 IGTP's Genomics Platform from tail samples. Both animal models were kept in the BSL-3
419 facility during the whole experiment including acclimatization period. The housing
420 conditions in the BSL-3 room were maintained as follows: a temperature of 22±2ºC,
421 humidity levels between 30-70%, 20 ACH, a 12h dark/light cycle, and access to food and
422 water *ad libitum.*

423 A total of 36 adult mice aged 5-11 months were used in this experiment, consisting of 32 KI
424 Col1a1-K18-hACE2 mice and 4 transgenic K18-hACE2 mice. All groups were sex balanced.
425 The infections were performed in two separate experiments between January and June
426 2022. Mice were anaesthetized with isoflurane (FDG9623; Baxter, Deerfield, IL, USA) and
427 infected with a B.1 isolate (27 Col1a1-K18-hACE2 and 4 K18-hACE2 mice). The uninfected
428 control group received PBS (5 Col1a1-K18-hACE2).

429 Infection was performed using 1,000 $TCID_{50}$ of B.1 SARS-CoV-2 isolate in 50 µl of PBS (25
430 µL/nostril), or PBS only (25 µL/nostril) for the control group. All mice fully recovered from
431 the challenge and anaesthesia procedures. Following the challenge, body weight and clinical
432 signs were monitored daily. Eight animals per group were euthanized at days 3, 7, 14 dpi or
433 upon fulfilment of human endpoint, for viral RNA quantification and histological analyses
434 (**Supplementary Table 2**). The endpoint criteria for animal welfare were established based

435 on a body weight loss of more than to 20% of the initial body weight and/or the display of
436 moderate to severe clinical signs (including neurological signs), in accordance with previous
437 studies (12–14). The evaluated clinical signs included respiration, physical appearance, lack
438 of responsiveness and neurological signs, that were scored from 0-2 depending on severity
439 (**Supplementary Table 1**). Euthanasia was performed under deep isoflurane anaesthesia by
440 whole blood extraction via cardiac puncture and cervical dislocation. Oropharyngeal swab,
441 lung, brain, and nasal turbinate were collected for viral and hACE2 RNA quantification,
442 histological and IHC analyses. For the latter techniques, tissues were fixed by immersion in
443 10% buffered formalin. An additional set of 9 tissues was collected to further characterize
444 the KI model both for viral RNA quantification and hACE2 receptor expression. These tissues
445 included muscle, intestine, liver, kidney, lymph nodes, spleen, heart, pancreas, and salivary
446 glands.

447 **Tissue sampling and processing**

448 The collected tissues were processed as described by Tarrés-Freixas et al. 2022 (13). Briefly,
449 approximately 100 mg of each tissue was collected in 1.5 mL Sarstedt tubes (72607;
450 Sarstedt, Nümbrecth, Germany) containing 500 µL of DMEM medium (11995065;
451 ThermoFisher Scientific) supplemented with 1% penicillin–streptomycin (10378016;
452 ThermoFisher Scientific). A 1.5 mm Tungsten bead (69997; QIAGEN, Hilden, Germany) was
453 added to each tube, and samples were homogenized twice at 25 Hz for 30 s using a
454 TissueLyser II (85300; QIAGEN) before being centrifuged for 2 min at 2,000 × g. Supernatants
455 were then stored at −80°C until the analysis of hACE2 expression and VL by RT-qPCR.

456 **hACE2 mRNA Expression**

457 RNA tissue extraction was performed by using the Viral RNA/ Pathogen Nucleic Acid
458 Isolation kit (A42352; ThermoFisher Scientific), optimized for use with a KingFisher
459 instrument (5400610; ThermoFisher Scientific), following the manufacturer's instructions.
460 The expression of hACE2 receptor in tissue was detected by RT-qPCR with a predefined
461 TaqMan assay with a ACE2 target (Hs01085333_m1, ThermoFisher Scientific). Mouse *gapdh*
462 gene expression was measured in duplicate for each sample using TaqMan®gene expression
463 assay (Mm99999915_g1; ThermoFisher Scientific) as amplification control. Data was
464 graphed both as the delta-Ct values of hACE2 minus GAPDH for each tissue, and the relative
465 expression of the receptor (delta-delta Ct value) of Col1a1-K18-hACE2 minus K18-hACE2
466 tissues.

467 **ACE2 Protein Expression**

468 ACE2 protein expression was assessed by WB. Tissue samples were obtained from
469 uninfected Col1a1-K18-hACE2, K18-hACE2 and WT mice and flash frozen. Frozen sections
470 of each tissue were sliced by cryostat processing (Leica CM1950). and homogenized in
471 100uL of RIPA buffer for 15 min on ice, followed by centrifugation at 1000g for 10 min.
472 Supernatant was then isolated, and total protein concentration was quantified by Pierce™
473 BCA Protein Assay (23225; ThermoFisher Scientific) following manufacturer's instructions.

474 For WB, 3 µg of lysate total protein (as quantified Pierce™ BCA Protein Assay (23225;
475 ThermoFisher Scientific) were run in NuPAGE Bis-Tris 4-12% acrylamide gels (NP0321;
476 ThermoFisher Scientific). BlueStar pre-stained protein ladder was used as a molecular
477 weight marker (523005; NIPPON Genetics, Tokyo, Japan). Proteins were blotted onto PVDF

478 membrane (Ref. 1704156; Bio-Rad) using the Trans-Blot Turbo Transfer System (Ref.
479 1704150 Bio-Rad) and membranes were blocked with EveryBlot Blocking Buffer (12010020;
480 Bio-Rad). Primary antibodies used were: Anti-hACE2 specific monoclonal (1:1000;
481 AB108209, Abcam) (20), Anti-ACE2 polyclonal (1:1000 AF933; R&D Systems) and Anti-
482 GAPDH (1:5000; Ab9485; Abcam). Secondary antibodies were: donkey anti-Rabbit (1:10000;
483 Ref. 711-036-152; Jackson Immunoresearch) or a donkey anti-Goat (1:10000; Ref. 705-035-
484 147; Jackson Immunoresearch). Membranes were developed with SuperSignal™ West
485 Femto Maximum Sensitivity Substrate (Ref. 34094; ThermoFisher Scientific) according to
486 the manufacturer's instructions and acquired with ChemiDOC™ MP Imaging System
487 (12003154; Bio-Rad). Images were processed and merged with ImageLab 6.0.1 software
488 (Bio-Rad).

489 **SARS-CoV-2 PCR Detection and Viral Load Quantification**

490 Viral RNA was quantified by RT-qPCR in both the standard set of samples (oropharyngeal
491 swab, lung, brain, and nasal turbinate), and the extended set (muscle, intestine, liver,
492 kidney, pancreas, salivary glands, lymph nodes and spleen).

493 RNA extraction was performed by using the Viral RNA/ Pathogen Nucleic Acid Isolation kit
494 (A42352; ThermoFisher Scientific), optimized for use with a KingFisher instrument
495 (5400610; ThermoFisher Scientific), following the manufacturer's instructions. PCR
496 amplification was based on the 2019-Novel Coronavirus Real-Time RT-PCR Diagnostic Panel
497 guidelines and protocol developed by the American Center for Disease Control and
498 Prevention (CDC-006-00019, v.07). Briefly, a 20 µL PCR reaction was set up containing 5 µL
499 of RNA, 1.5 µL of N2 primers and probe (2019-nCov CDC EUA Kit; catalog number 10006770;

500 Integrated DNA Technologies, Coralville, IA, USA) and 10 µl of GoTaq 1-Step RT-qPCR
501 (Promega, Madison, WI, USA). Thermal cycling was performed at 50°C for 15 min for reverse
502 transcription, followed by 95°C for 2 min and then 45 cycles of 95°C for 10 s, 56°C for 15 s
503 and 72°C for 30 s in the Applied Biosystems 7,500 or QuantStudio5 Real-Time PCR
504 instruments (ThermoFisher Scientific). For absolute quantification, a standard curve was
505 built using 1/5 serial dilutions of a SARS-CoV-2 plasmid (2019-nCoV_N_Positive Control;
506 catalog number 10006625, 200 copies/µL, Integrated DNA Technologies), which was run in
507 parallel with all PCR determinations. Viral RNA from each sample was quantified in
508 triplicate, and the mean viral RNA concentration (in copies/mL) was extrapolated from the
509 standard curve and corrected by the corresponding dilution factor. Mouse *gapdh* gene
510 expression was measured in duplicate for each sample using TaqMan®gene expression
511 assay (Mm99999915_g1; ThermoFisher Scientific) as amplification control.

512 **Viral Titration**

513 Lung tissues were evaluated for the presence of replicative virus by titration in Vero E6 cells
514 as previously described (14, 34, 35). Briefly, after tissue homogenization, each sample
515 underwent sequential 10-fold dilutions in duplicate, transferred onto a monolayer of Vero
516 E6 cell in a 96-well plate, and incubated at 37°C and 5% CO_2. Plates were monitored daily
517 under a microscope, and at 5 dpi, wells were evaluated for the presence of cytopathic
518 effects. The amount of infectious virus was calculated by determining the TCID50 using the
519 Reed–Muench method.

520 **Histological and Immunohistochemical Analyses**

521 Tissue samples were recovered at the designated endpoint (3,7,14 dpi or humane endpoint)
522 and fixed by immersion in 10% buffered formalin. Lung, nasal turbinate, and brain samples
523 were routinely processed for histological examination, with haematoxylin & eosin-stained
524 slides examined under an optical microscope in a blinded fashion. Brain was cut into two
525 coronal sections, including cerebellum/pons and hemispheres at thalamus level. A semi-
526 quantitative approach based on the amount of inflammation (none, mild, moderate, or
527 severe) was used to assess the damage caused by SARS-CoV-2 infection in mice, following a
528 previously published scoring system (14, 36). Additionally, an IHC technique was employed
529 to detect SARS-CoV-2 NP antigen in nasal turbinate, lung, and brain sections from all
530 animals, using a rabbit monoclonal antibody (40143-R019, Sino Biological, Beijing, China) at
531 a 1:15,000 dilution. The amount of viral antigen in tissues was semi-quantitatively scored in
532 a blinded fashion (low, moderate, and high amount, or lack of antigen detection) (14, 36).

533 **Cytokine Quantification**

534 To assess the viral-driven inflammation in lung in both animal models, the levels of IP-10,
535 IL-6, IFNγ, MCP-1 and MIP-1β cytokines were analyzed by Luminex in tissue extracts. Lung
536 samples were processed as described above and stored at -80ºC until analysis. In Col1a1-
537 K18-hACE2 mice, cytokines were analyzed at 3,7,14 dpi and those euthanized by humane
538 endpoint criteria (exitus). Uninfected Col1a1-K18-hACE2 and K18-hACE2 infected animals
539 were used as reference groups.

540 Cytokines were measured by Luminex xMAP technology and analyzed with xPONENT 3.1
541 software (Luminex Corporation) using the MCYTOMAG-70 kit, according to the

542 manufacturers' protocol with minor modifications. Briefly, after cytokine staining, samples
543 underwent an overnight incubation on a rocking shaker at 4°C, using 2% PFA to ensure
544 complete inactivation of any remaining SARS-CoV-2 particles; a fixation that does not alter
545 cytokine quantification (37). Before plate acquisition, the PFA was washed away and
546 replaced with sheath fluid.

547 **Pseudovirus generation and neutralization assay**

548 To assess the generation of neutralizing antibodies upon SARS-CoV-2 B.1 infection, we used
549 a previously described pseudovirus-based neutralization assay (38). Briefly, in Nunc 96-well
550 cell culture plates (Thermo Fisher Scientific), 200 TCID50 of a luciferase-reporter HIV-based
551 pseudovirus bearing the BA.1 SARS-CoV-2 spike were preincubated with four-fold serial
552 dilutions (1/60 - 1/61,440) of the heat-inactivated (56ºC for 30 minutes) serum samples, for
553 1 hour at 37ºC. Then $1x10^4$ HEK293T/hACE2 cells treated with DEAE-Dextran (Sigma-
554 Aldrich) were added. Results were read after 48 hours using the EnSight Multimode Plate
555 Reader and BriteLite Plus Luciferase reagent (PerkinElmer, USA). The values were
556 normalized, and the ID50 (reciprocal dilution inhibiting 50% of the infection)
557 were calculated as described (39).

558 **Statistical Analyses**

559 All figures were generated using GraphPad Prism 9.0.0. Statistical analyses were performed
560 using R v4.3. Survival Rates were estimated with Kaplan-Meier curves and compared with
561 the Log-rank test. Datasets with an abundance of data below the limit of detection, like VL,
562 were analyzed using the Peto-Peto Left-censored samples test with correction for multiple

563 comparisons. Histopathological, IHC scores and viral titrations were compared using an
564 Independence Asymptotic Generalized Pearson Chi-Squared Test for ordinal data. Cytokine
565 titers were compared by a Kruskal Wallis, with pairwise comparisons conducted using
566 Conover's non-parametric test.

567

Acknowledgements

The authors would like to acknowledge Jorge Díaz, Yaiza Rosales-Salgado, Rosa María Ampudia-Carrasco, Sergi Sunyé-Casas and Mireia Martínez from the CMCiB for their essential help in the BSL3 facility and the K18-hACE2 mouse colony. We also thank Marisa Larramona from Parc Científic de Barcelona for her invaluable help with the knock-in mouse colony. We thank the Dormeur Fondation for their financial support for the acquisition of the QuantStudio-5 real-time PCR system.

Author Contributions

AP-G, FT-F, BT, and JB conceived and designed the experiments. AP-G, FT-F, and BT performed the animal procedures. AP-G, FT-F, MP, ER-M, DR-R, DP-Z, JM-B, EP, JS, BT performed the analytical experiments. AP-G, B, JS, JV-A, VU and JB analyzed and interpreted the data. SF, BTondelli established and provided the Knock-in mouse colony. SC established communication between animal facilities and contributed to the veterinary report verification to allow the knock-in animal shipment to the CMCiB facility. DP-Z, JM-B, DR-R, NI-U provided key reagents. AP-G, BT, and JB wrote the paper. All authors contributed to the article and approved the submitted version.

Competing Interests /Funding

A.P-G was supported by a predoctoral grant from Generalitat de Catalunya and Fons Social Europeu (2022 FI_B 00698). This study was funded by Grifols, the Departament de Salut of the Generalitat de Catalunya (grant nos. SLD016 to J.B. and SLD015 to J.C.), the Spanish Health Institute Carlos III, CERCA Programme/Generalitat de Catalunya 2021 SGR 00452,

589 and the crowdfunding initiatives #joemcorono, BonPreu/Esclat, and Correos. NI-U is
590 supported by the Spanish Ministry of Science and Innovation (grants PID2023-147498OB-
591 I00, PID2020-117145RB-I00 and 10.13039/501100011033, Spain), EU HORIZON-HLTH-
592 2021CORONA-01 (grant 101046118, European Union) and by institutional funding of
593 Pharma Mar, Grifols, HIPRA, and Amassence. J. Blanco has received institutional funding
594 from Grífols, Nesapor Europe, HIPRA and MSD. Unrelated to the submitted work, J.B. and
595 J.C. are founders and shareholders of AlbaJuna Therapeutics, SL. B.C. is founder and
596 shareholder of AlbaJuna Therapeutics, SL, and AELIX Therapeutics, SL.

597 The funders had no role in study design, data collection and interpretation, or the decision
598 to submit the work for publication

599 **Data availability**

600 The data supporting the findings of this study are documented within the paper and are
601 available from the corresponding authors upon request.

602 **References**

603 1. Muñoz-Fontela C, Dowling WE, Funnell SGP, Gsell PS, Riveros-Balta AX, Albrecht RA,
604 Andersen H, Baric RS, Carroll MW, Cavaleri M, Qin C, Crozier I, Dallmeier K, de Waal
605 L, de Wit E, Delang L, Dohm E, Duprex WP, Falzarano D, Finch CL, Frieman MB,
606 Graham BS, Gralinski LE, Guilfoyle K, Haagmans BL, Hamilton GA, Hartman AL,
607 Herfst S, Kaptein SJF, Klimstra WB, Knezevic I, Krause PR, Kuhn JH, Le Grand R, Lewis
608 MG, Liu WC, Maisonnasse P, McElroy AK, Munster V, Oreshkova N, Rasmussen AL,
609 Rocha-Pereira J, Rockx B, Rodríguez E, Rogers TF, Salguero FJ, Schotsaert M,
610 Stittelaar KJ, Thibaut HJ, Tseng C Te, Vergara-Alert J, Beer M, Brasel T, Chan JFW,
611 García-Sastre A, Neyts J, Perlman S, Reed DS, Richt JA, Roy CJ, Segalés J, Vasan SS,
612 Henao-Restrepo AM, Barouch DH. 2020. Animal models for COVID-19. Nature
613 586:509–515.

614 2. Jackson CB, Farzan M, Chen B, Choe H. 2021. Mechanisms of SARS-CoV-2 entry into
615 cells. Nat Rev Mol Cell Biol 2021 231 23:3–20.

616 3. Hassan AO, Case JB, Winkler ES, Thackray LB, Kafai NM, Bailey AL, McCune BT, Fox
617 JM, Chen RE, Alsoussi WB, Turner JS, Schmitz AJ, Lei T, Shrihari S, Keeler SP,
618 Fremont DH, Greco S, McCray PB, Perlman S, Holtzman MJ, Ellebedy AH, Diamond
619 MS. 2020. A SARS-CoV-2 Infection Model in Mice Demonstrates Protection by
620 Neutralizing Antibodies. Cell 182:744-753.e4.

621 4. Tseng C-TK, Huang C, Newman P, Wang N, Narayanan K, Watts DM, Makino S,
622 Packard MM, Zaki SR, Chan T, Peters CJ. 2007. Severe Acute Respiratory Syndrome
623 Coronavirus Infection of Mice Transgenic for the Human Angiotensin-Converting
624 Enzyme 2 Virus Receptor. J Virol 81:1162–1173.

625 5. Jiang R Di, Liu MQ, Chen Y, Shan C, Zhou YW, Shen XR, Li Q, Zhang L, Zhu Y, Si HR,
626 Wang Q, Min J, Wang X, Zhang W, Li B, Zhang HJ, Baric RS, Zhou P, Yang X Lou, Shi
627 ZL. 2020. Pathogenesis of SARS-CoV-2 in Transgenic Mice Expressing Human
628 Angiotensin-Converting Enzyme 2. Cell 182:50-58.e8.

629 6. Bao L, Deng W, Huang B, Gao H, Liu J, Ren L, Wei Q, Yu P, Xu Y, Qi F, Qu Y, Li F, Lv Q,
630 Wang W, Xue J, Gong S, Liu M, Wang G, Wang S, Song Z, Zhao L, Liu P, Zhao L, Ye F,
631 Wang H, Zhou W, Zhu N, Zhen W, Yu H, Zhang X, Guo L, Chen L, Wang C, Wang Y,
632 Wang X, Xiao Y, Sun Q, Liu H, Zhu F, Ma C, Yan L, Yang M, Han J, Xu W, Tan W, Peng
633 X, Jin Q, Wu G, Qin C. 2020. The pathogenicity of SARS-CoV-2 in hACE2 transgenic
634 mice. Nat 2020 5837818 583:830–833.

635 7. Zhou B, Thao TTN, Hoffmann D, Taddeo A, Ebert N, Labroussaa F, Pohlmann A, King
636 J, Steiner S, Kelly JN, Portmann J, Halwe NJ, Ulrich L, Trüeb BS, Fan X, Hoffmann B,
637 Wang L, Thomann L, Lin X, Stalder H, Pozzi B, de Brot S, Jiang N, Cui D, Hossain J,
638 Wilson MM, Keller MW, Stark TJ, Barnes JR, Dijkman R, Jores J, Benarafa C,
639 Wentworth DE, Thiel V, Beer M. 2021. SARS-CoV-2 spike D614G change enhances
640 replication and transmission. Nature 592:122–127.

641 8. Winkler ES, Chen RE, Alam F, Yildiz S, Case JB, Uccellini MB, Holtzman MJ, Garcia-
642 Sastre A, Schotsaert M, Diamond MS. 2022. SARS-CoV-2 Causes Lung Infection
643 without Severe Disease in Human ACE2 Knock-In Mice. J Virol 96:e0151121.

644 9. McCray PB, Pewe L, Wohlford-Lenane C, Hickey M, Manzel L, Shi L, Netland J, Jia HP,
645 Halabi C, Sigmund CD, Meyerholz DK, Kirby P, Look DC, Perlman S. 2007. Lethal
646 Infection of K18- hACE2 Mice Infected with Severe Acute Respiratory Syndrome
647 Coronavirus . J Virol 81:813–821.

648 10. Zheng J, Wong LYR, Li K, Verma AK, Ortiz ME, Wohlford-Lenane C, Leidinger MR,
649 Knudson CM, Meyerholz DK, McCray PB, Perlman S. 2021. COVID-19 treatments
650 and pathogenesis including anosmia in K18-hACE2 mice. Nature 589:603–607.

651 11. Winkler ES, Bailey AL, Kafai NM, Nair S, McCune BT, Yu J, Fox JM, Chen RE, Earnest
652 JT, Keeler SP, Ritter JH, Kang LI, Dort S, Robichaud A, Head R, Holtzman MJ,
653 Diamond MS. 2020. SARS-CoV-2 infection of human ACE2-transgenic mice causes
654 severe lung inflammation and impaired function. Nat Immunol 2020 2111 21:1327–
655 1335.

656 12. Carossino M, Kenney D, O'Connell AK, Montanaro P, Tseng AE, Gertje HP, Grosz KA,
657 Ericsson M, Huber BR, Kurnick SA, Subramaniam S, Kirkland TA, Walker JR, Francis
658 KP, Klose AD, Paragas N, Bosmann M, Saeed M, Balasuriya UBR, Douam F, Crossland
659 NA. 2022. Fatal Neurodissemination and SARS-CoV-2 Tropism in K18-hACE2 Mice Is
660 Only Partially Dependent on hACE2 Expression. Viruses 14:535.

661 13. Tarrés-Freixas F, Trinité B, Pons-Grífols A, Romero-Durana M, Riveira-Muñoz E,
662 Ávila-Nieto C, Pérez M, Garcia-Vidal E, Perez-Zsolt D, Muñoz-Basagoiti J, Raïch-
663 Regué D, Izquierdo-Useros N, Andrés C, Antón A, Pumarola T, Blanco I, Noguera-
664 Julián M, Guallar V, Lepore R, Valencia A, Urrea V, Vergara-Alert J, Clotet B, Ballana
665 E, Carrillo J, Segalés J, Blanco J. 2022. Heterogeneous Infectivity and Pathogenesis of
666 SARS-CoV-2 Variants Beta, Delta and Omicron in Transgenic K18-hACE2 and
667 Wildtype Mice. Front Microbiol 13:840757.

668 14. Vidal E, López-Figueroa C, Rodon J, Pérez M, Brustolin M, Cantero G, Guallar V,
669 Izquierdo-Useros N, Carrillo J, Blanco J, Clotet B, Vergara-Alert J, Segalés J, E V, C L-F,
670 J R, M P, M B, G C, V G, N I-U, J C, J B, B C, J V-A, J S. 2021. Chronological brain
671 lesions after SARS-CoV-2 infection in hACE2-transgenic mice. Vet Pathol 59:613–
672 626.

673 15. Shuai H, Chan JF-W, Yuen TT-T, Yoon C, Hu J-C, Wen L, Hu B, Yang D, Wang Y, Hou Y,
674 Huang X, Chai Y, Chan CC-S, Poon VK-M, Lu L, Zhang R-Q, Chan W-M, Ip JD, Chu AW-
675 H, Hu Y-F, Cai J-P, Chan K-H, Zhou J, Sridhar S, Zhang B-Z, Yuan S, Zhang AJ, Huang J-
676 D, To KK-W, Yuen K-Y, Chu H. 2021. Emerging SARS-CoV-2 variants expand species
677 tropism to murines. EBioMedicine 73:103643.

678 16. Netland J, Meyerholz DK, Moore S, Cassell M, Perlman S. 2008. Severe Acute
679 Respiratory Syndrome Coronavirus Infection Causes Neuronal Death in the Absence
680 of Encephalitis in Mice Transgenic for Human ACE2. J Virol 82:7264–7275.

681 17. Meinhardt J, Streit S, Dittmayer C, Manitius R v., Radbruch H, Heppner FL. 2023. The
682 neurobiology of SARS-CoV-2 infection. Nat Rev Neurosci 2023 251 25:30–42.

683 18. Matschke J, Lütgehetmann M, Hagel C, Sperhake JP, Schröder AS, Edler C,
684 Mushumba H, Fitzek A, Allweiss L, Dandri M, Dottermusch M, Heinemann A,
685 Pfefferle S, Schwabenland M, Sumner Magruder D, Bonn S, Prinz M, Gerloff C,
686 Püschel K, Krasemann S, Aepfelbacher M, Glatzel M. 2020. Neuropathology of
687 patients with COVID-19 in Germany: a post-mortem case series. Lancet Neurol
688 19:919–929.

689 19. Beard C, Hochedlinger K, Plath K, Wutz A, Jaenisch R. 2006. Efficient method to
690 generate single-copy transgenic mice by site-specific integration in embryonic stem
691 cells. genesis 44:23–28.

692 20. Sun SH, Chen Q, Gu HJ, Yang G, Wang YX, Huang XY, Liu SS, Zhang NN, Li XF, Xiong R,
693 Guo Y, Deng YQ, Huang WJ, Liu Q, Liu QM, Shen YL, Zhou Y, Yang X, Zhao TY, Fan CF,
694 Zhou Y Sen, Qin CF, Wang YC. 2020. A Mouse Model of SARS-CoV-2 Infection and
695 Pathogenesis. Cell Host Microbe 28:124-133.e4.

696 21. Yinda CK, Port JR, Bushmaker T, Owusu IO, Purushotham JN, Avanzato VA, Fischer
697 RJ, Schulz JE, Holbrook MG, Hebner MJ, Rosenke R, Thomas T, Marzi A, Best SM, de
698 Wit E, Shaia C, van Doremalen N, Munster VJ. 2021. K18-hACE2 mice develop
699 respiratory disease resembling severe COVID-19. PLOS Pathog 17:e1009195.

700 22. Bradshaw CM, Georgieva T, Tankersley TN, Taylor-Doyle T, Johnson L, Uhrlaub JL,
701 Besselsen D, Nikolich JŽ. 2024. Cutting Edge: Characterization of Low Copy Number
702 Human Angiotensin-Converting Enzyme 2–Transgenic Mice as an Improved Model
703 of SARS-CoV-2 Infection. J Immunol 212:523–528.

704 23. Dong W, Mead H, Tian L, Park J-G, Garcia JI, Jaramillo S, Barr T, Kollath DS, Coyne
705 VK, Stone NE, Jones A, Zhang J, Li A, Wang L-S, Milanes-Yearsley M, Torrelles JB,
706 Martinez-Sobrido L, Keim PS, Barker BM, Caligiuri MA, Yu J. 2022. The K18-Human
707 ACE2 Transgenic Mouse Model Recapitulates Non-severe and Severe COVID-19 in
708 Response to an Infectious Dose of the SARS-CoV-2 Virus. J Virol 96:e0096421.

709 24. Hikmet F, Méar L, Edvinsson Å, Micke P, Uhlén M, Lindskog C. 2020. The protein
710 expression profile of ACE2 in human tissues. Mol Syst Biol 16:e9610.

711 25. Barut GT, Halwe NJ, Taddeo A, Kelly JN, Schön J, Ebert N, Ulrich L, Devisme C,
712 Steiner S, Trüeb BS, Hoffmann B, Veiga IB, Leborgne NGF, Moreira EA, Breithaupt A,
713 Wylezich C, Höper D, Wernike K, Godel A, Thomann L, Flück V, Stalder H, Brügger M,
714 Esteves BIO, Zumkehr B, Beilleau G, Kratzel A, Schmied K, Ochsenbein S, Lang RM,
715 Wider M, Machahua C, Dorn P, Marti TM, Funke-Chambour M, Rauch A, Widera M,
716 Ciesek S, Dijkman R, Hoffmann D, Alves MP, Benarafa C, Beer M, Thiel V. 2022. The
717 spike gene is a major determinant for the SARS-CoV-2 Omicron-BA.1 phenotype.
718 Nat Commun 13:5929.

719 26. Oladunni FS, Park J-G, Pino PA, Gonzalez O, Akhter A, Allué-Guardia A, Olmo-

720 Fontánez A, Gautam S, Garcia-Vilanova A, Ye C, Chiem K, Headley C, Dwivedi V,
721 Parodi LM, Alfson KJ, Staples HM, Schami A, Garcia JI, Whigham A, Platt RN, Gazi M,
722 Martinez J, Chuba C, Earley S, Rodriguez OH, Mdaki SD, Kavelish KN, Escalona R,
723 Hallam CRA, Christie C, Patterson JL, Anderson TJC, Carrion R, Dick EJ, Hall-Ursone S,
724 Schlesinger LS, Alvarez X, Kaushal D, Giavedoni LD, Turner J, Martinez-Sobrido L,
725 Torrelles JB. 2020. Lethality of SARS-CoV-2 infection in K18 human angiotensin-
726 converting enzyme 2 transgenic mice. Nat Commun 11:6122.

727 27. Fumagalli V, Ravà M, Marotta D, Di Lucia P, Laura C, Sala E, Grillo M, Bono E,
728 Giustini L, Perucchini C, Mainetti M, Sessa A, Garcia-Manteiga JM, Donnici L,
729 Manganaro L, Delbue S, Broccoli V, De Francesco R, D'Adamo P, Kuka M, Guidotti
730 LG, Iannacone M. 2022. Administration of aerosolized SARS-CoV-2 to K18-hACE2
731 mice uncouples respiratory infection from fatal neuroinvasion. Sci Immunol
732 7:eabl9929.

733 28. Radvak P, Kwon HJ, Kosikova M, Ortega-Rodriguez U, Xiang R, Phue JN, Shen RF,
734 Rozzelle J, Kapoor N, Rabara T, Fairman J, Xie H. 2021. SARS-CoV-2 B.1.1.7 (alpha)
735 and B.1.351 (beta) variants induce pathogenic patterns in K18-hACE2 transgenic
736 mice distinct from early strains. Nat Commun 12:1–15.

737 29. Case JB, Scheaffer SM, Darling TL, Bricker TL, Adams LJ, Harastani HH, Trende R,
738 Sanapala S, Fremont DH, Boon ACM, Diamond MS. 2023. Characterization of the
739 SARS-CoV-2 BA.5.5 and BQ.1.1 Omicron variants in mice and hamsters. J Virol
740 97:e0062823.

741 30. Halfmann PJ, Iida S, Iwatsuki-Horimoto K, Maemura T, Kiso M, Scheaffer SM, Darling
742 TL, Joshi A, Loeber S, Singh G, Foster SL, Ying B, Case JB, Chong Z, Whitener B,
743 Moliva J, Floyd K, Ujie M, Nakajima N, Ito M, Wright R, Uraki R, Warang P, Gagne M,
744 Li R, Sakai-Tagawa Y, Liu Y, Larson D, Osorio JE, Hernandez-Ortiz JP, Henry AR,
745 Ciuoderis K, Florek KR, Patel M, Odle A, Wong L-YR, Bateman AC, Wang Z, Edara V-
746 V, Chong Z, Franks J, Jeevan T, Fabrizio T, DeBeauchamp J, Kercher L, Seiler P,
747 Gonzalez-Reiche AS, Sordillo EM, Chang LA, van Bakel H, Simon V, Consortium
748 Mount Sinai Pathogen Surveillance (PSP) study group, Douek DC, Sullivan NJ,
749 Thackray LB, Ueki H, Yamayoshi S, Imai M, Perlman S, Webby RJ, Seder RA, Suthar
750 MS, García-Sastre A, Schotsaert M, Suzuki T, Boon ACM, Diamond MS, Kawaoka Y.
751 2022. SARS-CoV-2 Omicron virus causes attenuated disease in mice and hamsters.
752 Nature 603:687–692.

753 31. Stewart R, Yan K, Ellis SA, Bishop CR, Dumenil T, Tang B, Nguyen W, Larcher T, Parry
754 R, Sng JDJ, Khromykh AA, Sullivan RKP, Lor M, Meunier FA, Rawle DJ, Suhrbier A.
755 2023. SARS-CoV-2 omicron BA.5 and XBB variants have increased neurotropic
756 potential over BA.1 in K18-hACE2 mice and human brain organoids. Front Microbiol
757 14:1320856.

758 32. Zhang Z, Zhou L, Liu Q, Zheng Y, Tan X, Huang Z, Guo M, Wang X, Chen X, Liang S, Li
759 W, Song K, Yan K, Li J, Li Q, Zhang Y, Yang S, Cai Z, Dai M, Xian Q, Shi Z-L, Xu K, Lan K,
760 Chen Y. 2024. The lethal K18-hACE2 knock-in mouse model mimicking the severe

761 pneumonia of COVID-19 is practicable for antiviral development. Emerg Microbes
762 Infect 13:2353302.

763 33. Perez-Zsolt D, Muñoz-Basagoiti J, Rodon J, Elousa M, Raïch-Regué D, Risco C, Sachse
764 M, Pino M, Gumber S, Paiardini M, Chojnacki J, Erkizia I, Muñiz X, Ballana E, Riveira-
765 Muñoz E, Noguera M, Paredes R, Trinité B, Tarrés-Freixas F, Blanco I, Guallar V,
766 Carrillo J, Blanco J, Telenti A, Heyn H, Segalés J, Clotet B, Martinez-Picado J, Vergara-
767 Alert J, Izquierdo-Useros N. 2021. Siglec-1 on dendritic cells mediates SARS-CoV-2
768 trans -infection of target cells while on macrophages triggers proinflammatory
769 responses. bioRxiv. Cold Spring Harbor Laboratory
770 https://doi.org/10.1101/2021.05.11.443572.

771 34. Rodon J, Muñoz-Basagoiti J, Perez-Zsolt D, Noguera-Julian M, Paredes R, Mateu L,
772 Quiñones C, Perez C, Erkizia I, Blanco I, Valencia A, Guallar V, Carrillo J, Blanco J,
773 Segalés J, Clotet B, Vergara-Alert J, Izquierdo-Useros N. 2021. Identification of
774 Plitidepsin as Potent Inhibitor of SARS-CoV-2-Induced Cytopathic Effect After a Drug
775 Repurposing Screen. Front Pharmacol 12:646676.

776 35. Haagmans BL, van den Brand JMA, Raj VS, Volz A, Wohlsein P, Smits SL, Schipper D,
777 Bestebroer TM, Okba N, Fux R, Bensaid A, Solanes Foz D, Kuiken T, Baumgärtner W,
778 Segalés J, Sutter G, Osterhaus ADME. 2016. An orthopoxvirus-based vaccine
779 reduces virus excretion after MERS-CoV infection in dromedary camels. Science (80-
780) 351:77–81.

781 36. Brustolin M, Rodon J, Rodríguez de la Concepción ML, Ávila-Nieto C, Cantero G,
782 Pérez M, Te N, Noguera-Julián M, Guallar V, Valencia A, Roca N, Izquierdo-Useros N,
783 Blanco J, Clotet B, Bensaid A, Carrillo J, Vergara-Alert J, Segalés J. 2021. Protection
784 against reinfection with D614- or G614-SARS-CoV-2 isolates in golden Syrian
785 hamster. Emerg Microbes Infect 10:797.

786 37. Dowall SD, Graham VA, Tipton TRW, Hewson R. 2009. Multiplex cytokine profiling
787 with highly pathogenic material: use of formalin solution in luminex analysis. J
788 Immunol Methods 348:30–35.

789 38. Pradenas E, Trinité B, Urrea V, Marfil S, Ávila-Nieto C, Rodríguez de la Concepción
790 ML, Tarrés-Freixas F, Pérez-Yanes S, Rovirosa C, Ainsua-Enrich E, Rodon J, Vergara-
791 Alert J, Segalés J, Guallar V, Valencia A, Izquierdo-Useros N, Paredes R, Mateu L,
792 Chamorro A, Massanella M, Carrillo J, Clotet B, Blanco J. 2021. Stable neutralizing
793 antibody levels 6 months after mild and severe COVID-19 episodes. Med 2:313-
794 320.e4.

795 39. Trinité B, Tarrés-Freixas F, Rodon J, Pradenas E, Urrea V, Marfil S, Rodríguez de la
796 Concepción ML, Ávila-Nieto C, Aguilar-Gurrieri C, Barajas A, Ortiz R, Paredes R,
797 Mateu L, Valencia A, Guallar V, Ruiz L, Grau E, Massanella M, Puig J, Chamorro A,
798 Izquierdo-Useros N, Segalés J, Clotet B, Carrillo J, Vergara-Alert J, Blanco J. 2021.
799 SARS-CoV-2 infection elicits a rapid neutralizing antibody response that correlates
800 with disease severity. Sci Rep 11:2608.

804 **Figure Legends**

805 **Figure 1. Expression of hACE2 in the Col1a1-K18-hACE2 KI model.** (A) Schematic
806 representation of the insertion strategy. The original K18-hACE2 transgene was inserted
807 into the collagen COL1A1 locus using a recombinase mediated cassette exchange (RMCE)
808 FLP-FRT system in KH2 cells via blastocyst injection. pPGK-ATG-frt plasmid: vector backbone
809 with Ampicillin resistant gene (Amp), transcription start site (ATG) and Flippase recognition
810 target (Frt). Hygro: Hygromicin resistance gene. pCAGGS-FlpE: expression plasmid for FLPe
811 recombinase expression. (B) Relative quantification of hACE2 receptor expression to GAPDH
812 expression in uninfected Col1a1-K18-hACE2 ((blue empty dot, n=3) and K18-hACE2 males
813 (black empty square, n=3). Delta Ct values are inversely shown to facilitate interpretation.
814 The lower the absolute number, the higher the relative expression. Solid line and bars
815 represent mean and SEM. (C) Relative comparison of hACE2 receptor expression in Col1a1-
816 K18-hACE2 versus K18-hACE2 mice (n=3 each, males). Higher receptor expression in Col1a1-
817 K18-hACE2 (negative values in Y axis) is marked by blue bars, and higher expression in K18-
818 hACE2 (positive values in Y axis) is marked in black bars. (D) Western Blot analysis of hACE2,
819 mACE2 and GAPDH in representative tissues. hACE2 signal was obtained using a specific
820 monoclonal antibody (top panels); mACE2 and hACE2 signal was obtained with a cross-
821 reactive polyclonal antibody (middle panel), and anti-GAPDH was analyzed as reference
822 (bottom panels). Molecular weight marker is shown on the right.

823 **Figure 2. Experimental setting and progression of SARS-CoV-2 infection in Col1a1-K18-**
824 **hACE2 and K18-hACE2 mouse models.** (A) Schematic representation of the experimental
825 setting. Knock-in Col1a1-K18-hACE2 (n=27) and transgenic K18-hACE2 mice (n=4) were

826 intranasally challenged with a 1000 $TCID_{50}$ dose of a B.1 SARS-CoV-2 isolate. A Col1a1-K18-
827 hACE2 uninfected control group (n=5) was challenged with PBS. Mice were monitored for
828 weight-loss and clinical signs for 14 days post infection (dpi). Euthanasia was performed at
829 3, 7, and 14 dpi or upon fulfilment of humane endpoint criteria, for sample and tissue
830 collection (n=8 per timepoint). Infections were performed in two separate experiments
831 between January and June 2022. Created with Biorender.com. (B) Relative body weight
832 follow-up referred to day 0. Col1a1-K18-hACE2 uninfected (blue empty dot), Col1a1-K18-
833 hACE2 infected (blue dot), K18-hACE2 infected (black square). Solid lines and bars represent
834 mean±SD. (C) Survival (Kaplan-Meier). All K18-hACE2 infected animals (n=4) had to be
835 euthanized due to endpoint criteria by 7dpi, and only three infected Col1a1-K18-hACE2 at
836 8, 9, and 10 dpi. No uninfected Col1a1-K18-hACE2 had to be euthanized under this criterion.
837 Col1a1-K18-hACE2 uninfected (blue dashed line), Col1a1-K18-hACE2 infected (blue line),
838 K18-hACE2 infected (black line). Statistical differences were identified using a Log-rank
839 (Mantel-Cox) test (<0.0001), followed by individual comparisons (**$p < 0.005$; ****$p <$
840 0.0001)

841 **Figure 3. Progression of SARS-CoV-2 infection in Col1a1-K18-hACE2 KI mice.** Col1a1-K18-
842 hACE2 (blue circles, *n=27*) and K18-hACE2+ mice (black squares, *n=4*) were inoculated with
843 1000 $TCID_{50}$ of a SARS-CoV-2 B.1 isolate (full shapes) or uninfected (empty shapes of each
844 colour, *n=5*). Animals were euthanized at 3dpi (n=8), 7dpi (n=8), 14 dpi (n=8) or upon
845 fulfilment of humane endpoint criteria **(n=3, euthanized at 8,9 and 10 dpi)**. (A) SARS-CoV-2
846 viral RNA loads (copies/mL) of oropharyngeal swab, lung, and nasal turbinate samples.
847 Dashed line represents limit of detection, established by 2SD of uninfected animals.

848 Statistical differences were identified using a Peto-Peto Left censored test (*p < 0.05,
849 **p<0.005). (B) Viral titration of replicative virus ($TCID_{50}$/mL) in lung samples from B.1
850 infected mice at different endpoints in Vero E6 cells on day 5 of culture. Titers were
851 compared using an Independence Asymptotic Generalized Pearson Chi-Squared Test for
852 ordinal data (*p < 0.05, **p<0.005). (C) Lung histopathological scoring of broncho-
853 interstitial pneumonia (left) and SARS-CoV-2 NP immunohistochemical (IHC) scoring (right)
854 in both models at 3, 7, 14 dpi and endpoint. Statistical differences were identified using an
855 Independence Asymptotic Generalized Pearson Chi-Squared Test for ordinal data (*p <
856 0.05). (D) Representative lung histology and IHC pictures of both models at 3, 7, 14 dpi and
857 endpoint. Images show low-power magnification bars (200 µm).

858 **Figure 4. Inflammatory response in the lung.** The concentration of Inflammatory cytokines
859 in lung extracts in the knock-in and transgenic models at 3,7,14 dpi or endpoint are shown.
860 Col1a1-K18-hACE2 infected (blue full circles, *n=23*), uninfected (blue empty circles, n=3) and
861 K18-hACE2 infected mice (black full squares, *n=4*). The bar shows Median with interquartile
862 range. The limit of detection for each cytokine is indicated by a dotted line. Statistical
863 differences were identified using a Kruskal Wallis, and a Conover's nonparametric all-pairs
864 comparison test (*p < 0.05, **p<0.005).

865 **Figure 5. Tissue Tropism of SARS-CoV-2 in Col1a1-K18-hACE2 and K18-hACE2 Mice.** SARS-
866 CoV-2 viral RNA loads (copies/mL) were analyzed by RT-qPCR in Col1a1-K18-hACE2 mice
867 tissues collected at 3,7 and 14 dpi (n=3 per timepoint) or upon fulfilment of humane
868 endpoint criteria (n=1 at 8 dpi, n=1 at 9 dpi). K18-hACE2 tissues were collected at endpoint

869 at 6 (n=1) and 7 dpi (n=1). Solid lines show the mean ±SD. Dashed line represents limit of
870 detection, established by 2SD of uninfected animals.

871 **Figure 6. Progression of SARS-CoV-2 infection in brain from the Col1a1-K18-hACE2 KI mice.**
872 Col1a1-K18-hACE2 (blue circles, *n=27*) and K18-hACE2+ mice (black squares, *n=4*) were
873 inoculated with 1000 $TCID_{50}$ of a B.1 SARS-CoV-2 isolate (full shapes) or uninfected (empty
874 shapes, *n=5*) and followed until 14 dpi. Samples were collected at 3, 7, 14 dpi and endpoint.
875 (A) SARS-CoV-2 viral RNA loads (copies/mL) in brain extracts. Dashed line represents limit
876 of detection, established by 2SD of uninfected animals. Statistical differences were
877 identified using a Peto-Peto Left-censored samples test with correction for multiple
878 comparisons. Solid line and bars represent mean and SD. (B) Viral titration of replicative
879 virus ($TCID_{50/}$mL) in brain samples from B.1 infected mice at different endpoints in Vero E6
880 cells on day 5 of culture. Solid line and bars represent mean and SD. (C) Brain
881 histopathological scoring of multifocal lymphoplasmacytic meningo-encephalitis in brain
882 (Left) and SARS-CoV-2 NP IHC scoring (right) in brain of both models. Statistical differences
883 were identified using an Independence Asymptotic Generalized Pearson Chi-Squared Test
884 for ordinal data (*$p < 0.05$; **$p < 0.01$). (D) Representative images of brain Histology and
885 IHC images of both hACE2+ mouse models. Images show low-power magnification (top;
886 bars: 600µm) and medium-power magnification (bottom; bars: 300µm). Col1a1-K18-hACE2
887 KI mice samples shown were collected at 7 dpi, while K18-hACE2 samples were collected at
888 humane endpoint (6-7dpi).

A

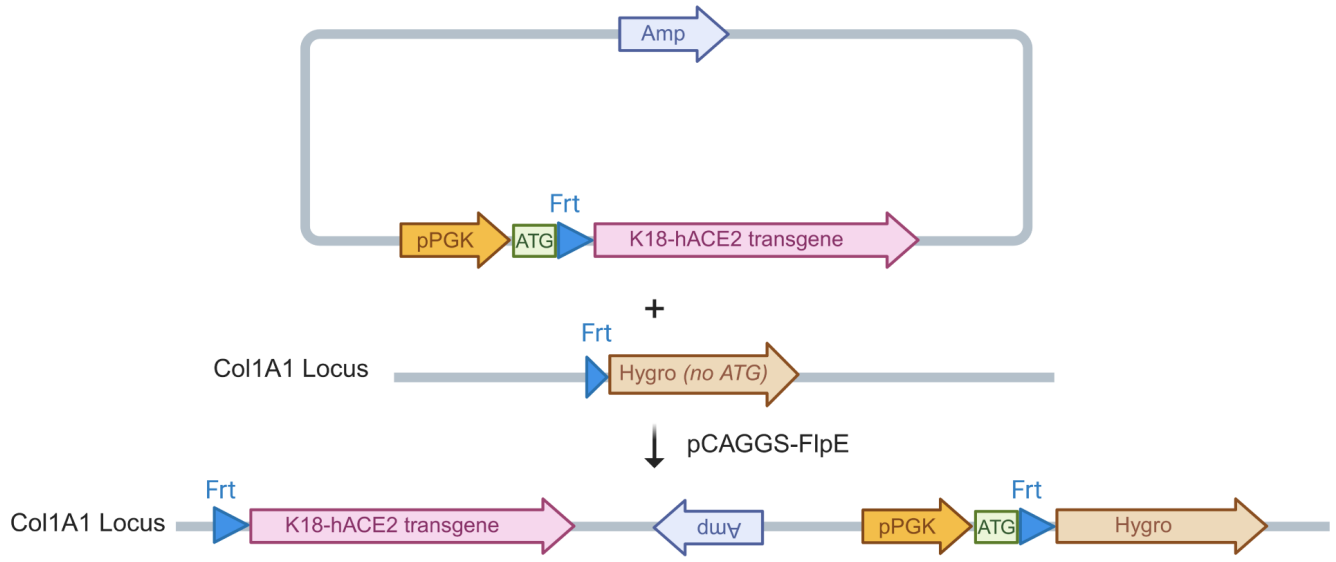
Amp
Frt
pPGK
ATG
K18-hACE2 transgene
+
Frt
Col1A1 Locus
Hygro (no ATG)
pCAGGS-FlpE
Frt
Col1A1 Locus
K18-hACE2 transgene
Amp
pPGK
ATG
Frt
Hygro

B

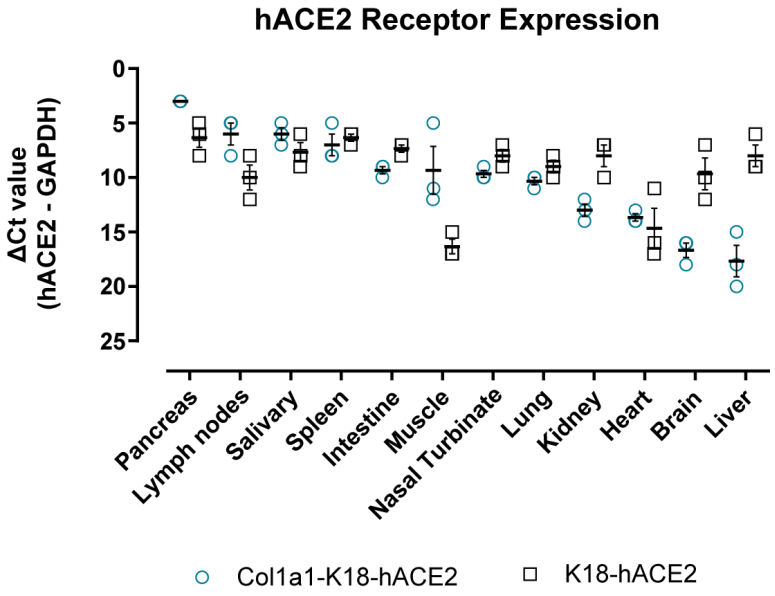
hACE2 Receptor Expression
ΔCt value
(hACE2 - GAPDH)
0
5
10
15
20
25
Pancreas
Lymph nodes
Salivary
Spleen
Intestine
Muscle
Nasal Turbinate
Lung
Kidney
Heart
Brain
Liver
Col1a1-K18-hACE2
K18-hACE2

C

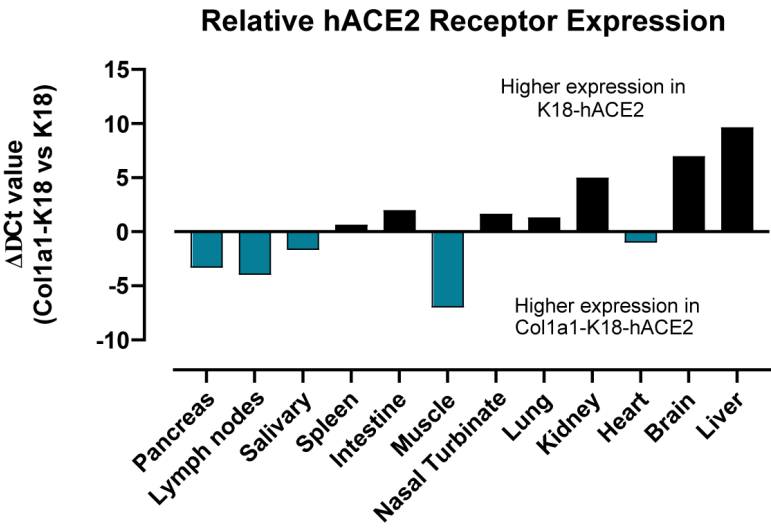
Relative hACE2 Receptor Expression
ΔDCt value
(Col1a1-K18 vs K18)
15
10
5
0
-5
-10
Higher expression in
K18-hACE2
Higher expression in
Col1a1-K18-hACE2
Pancreas
Lymph nodes
Salivary
Spleen
Intestine
Muscle
Nasal Turbinate
Lung
Kidney
Heart
Brain
Liver

D

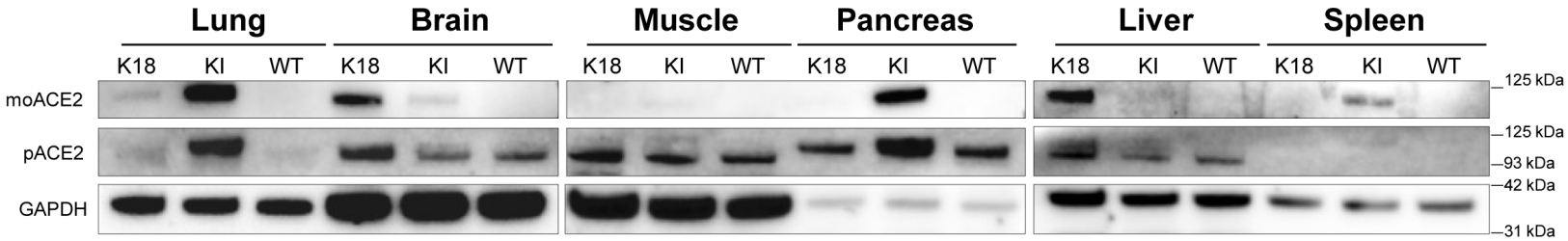
Lung
Brain
Muscle
Pancreas
Liver
Spleen
K18
KI
WT
moACE2
pACE2
GAPDH
125 kDa
125 kDa
93 kDa
42 kDa
31 kDa

A

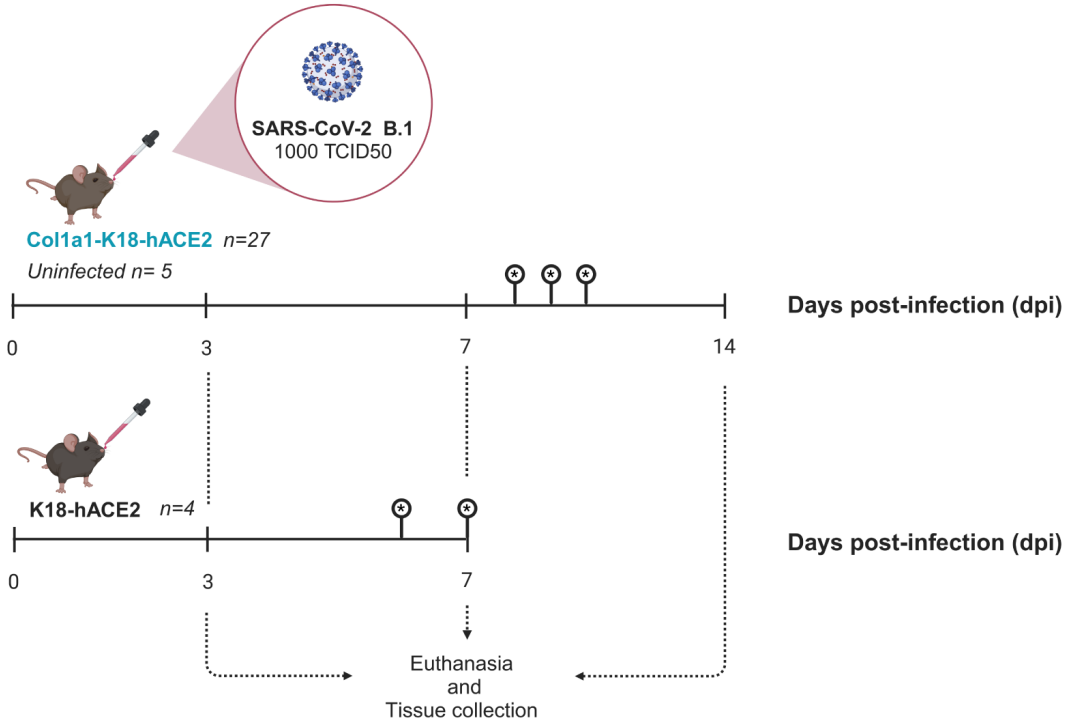
SARS-CoV-2 B.1
1000 TCID50
Col1a1-K18-hACE2 n=27
Uninfected n= 5
Days post-infection (dpi)
0
3
7
14
K18-hACE2 n=4
Days post-infection (dpi)
0
3
7
Euthanasia
and
Tissue collection

B

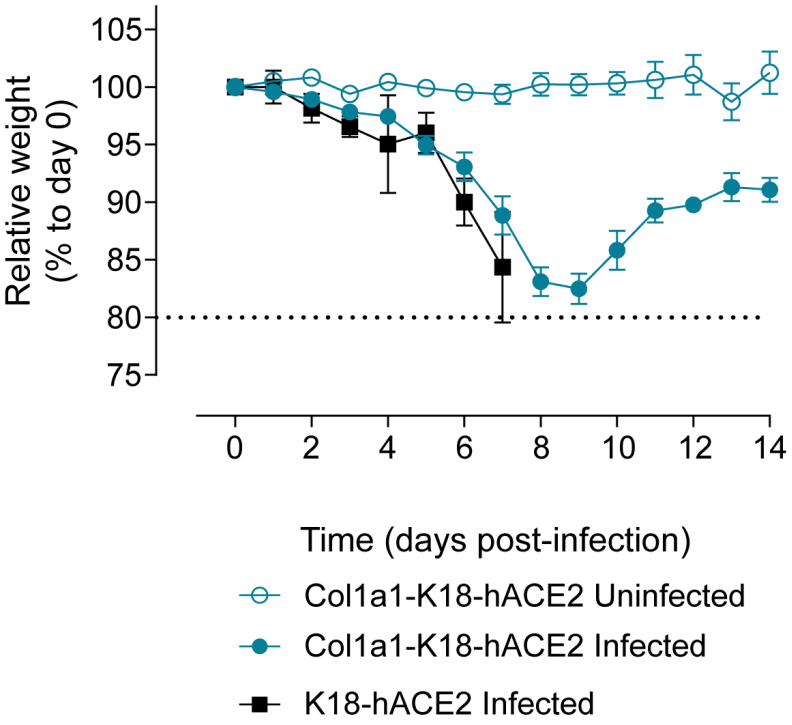
Relative weight
(% to day 0)
105
100
95
90
85
80
75
0
2
4
6
8
10
12
14
Time (days post-infection)
Col1a1-K18-hACE2 Uninfected
Col1a1-K18-hACE2 Infected
K18-hACE2 Infected

C

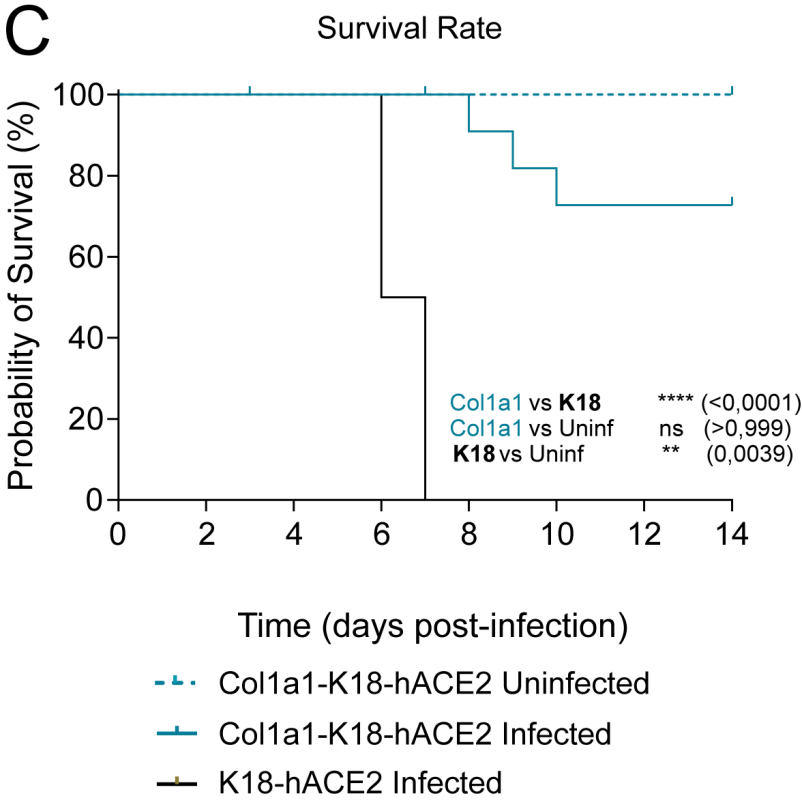
Survival Rate
Probability of Survival (%)
100
80
60
40
20
0
0
2
4
6
8
10
12
14
Col1a1 vs K18 **** (<0,0001)
Col1a1 vs Uninf ns (>0,999)
K18 vs Uninf ** (0,0039)
Time (days post-infection)
Col1a1-K18-hACE2 Uninfected
Col1a1-K18-hACE2 Infected
K18-hACE2 Infected

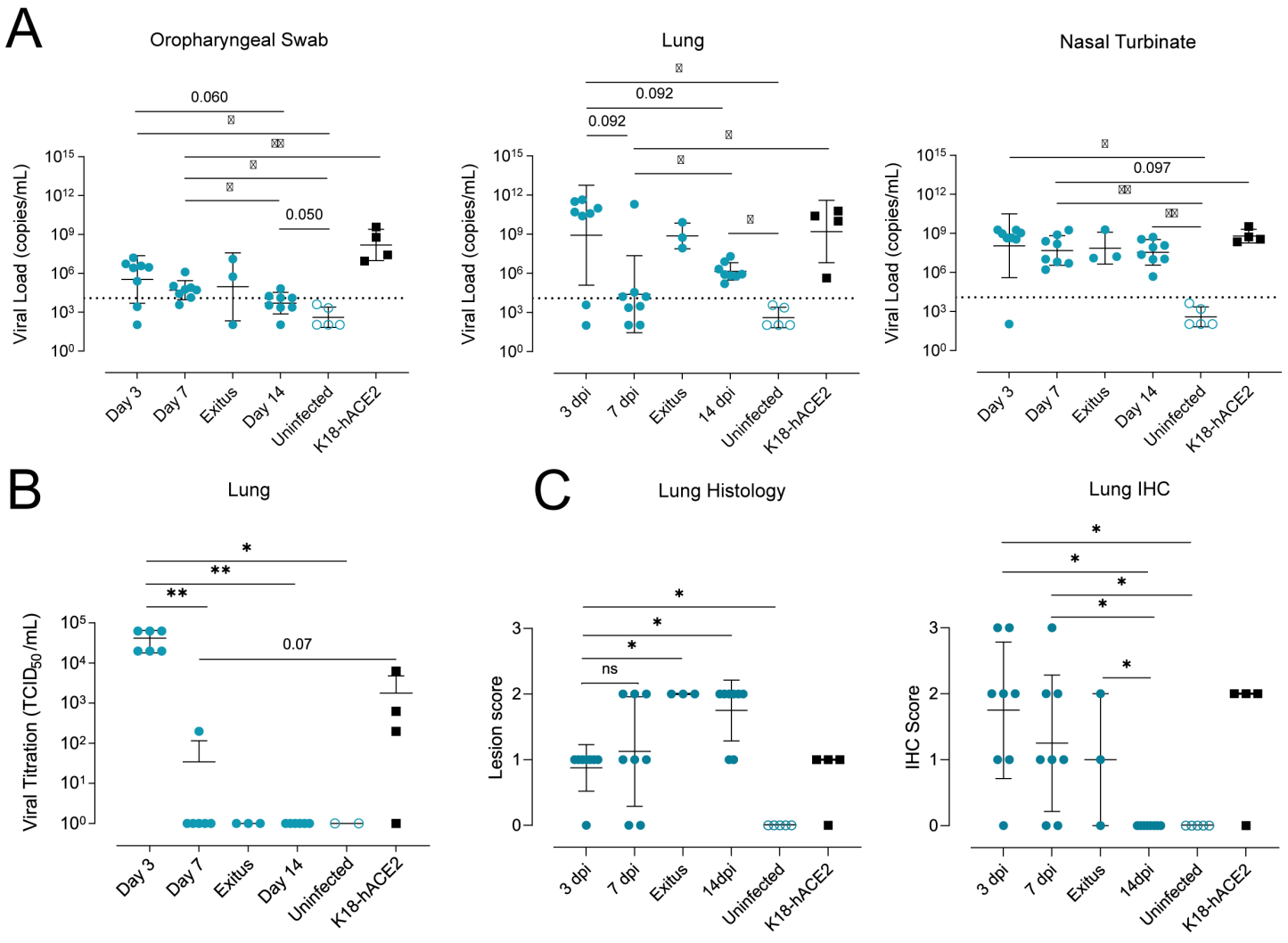
A
Oropharyngeal Swab
Lung
Nasal Turbinate
Viral Load (copies/mL)
0.060
0.050
0.092
0.092
0.097
Day 3
Day 7
Exitus
Day 14
Uninfected
K18-hACE2
3 dpi
7 dpi
14 dpi
B
Lung
Viral Titration (TCID50/mL)
0.07
C
Lung Histology
Lung IHC
Lesion score
IHC Score
ns
14dpi

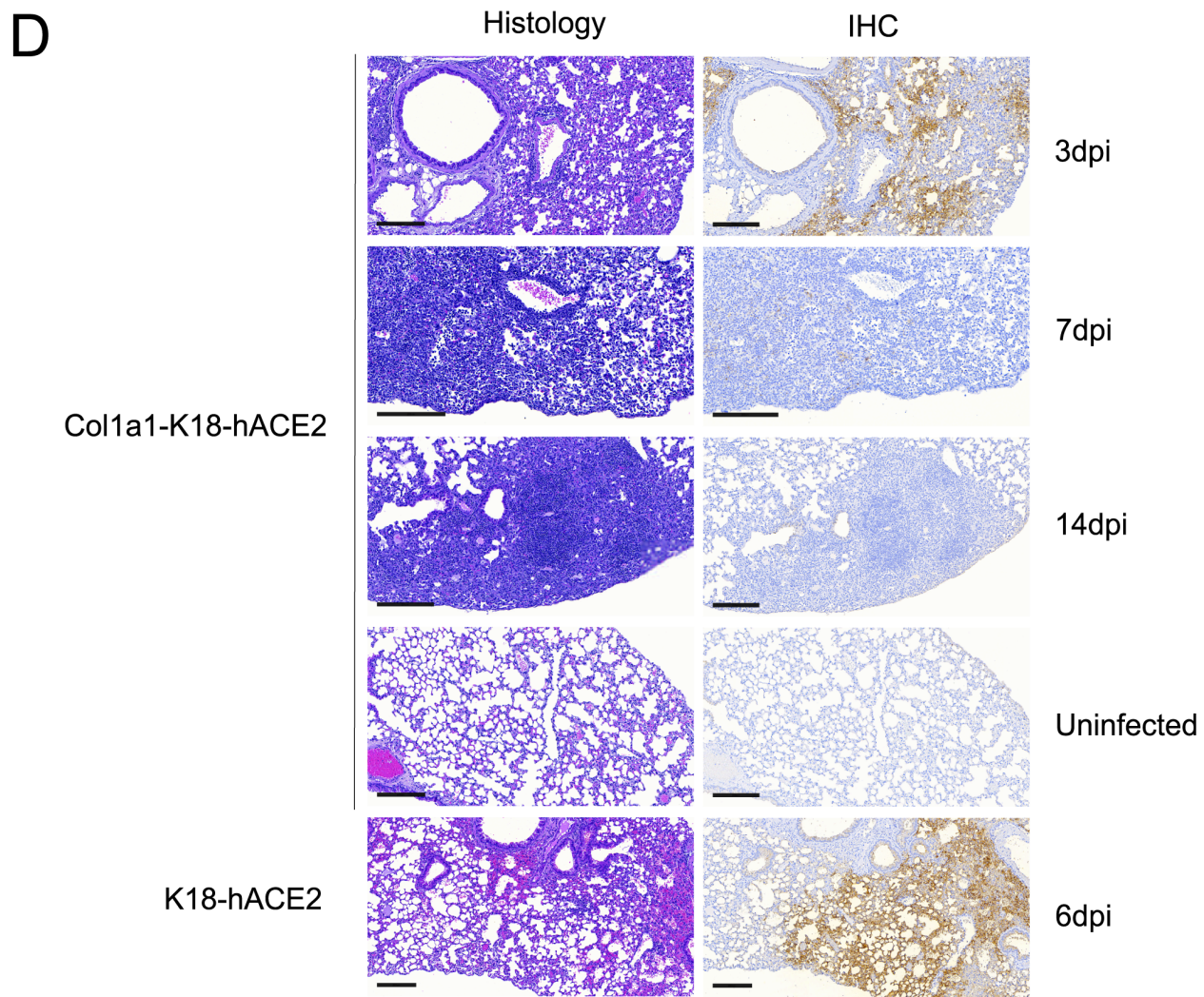
D
Histology
IHC
3dpi
7dpi
14dpi
Uninfected
6dpi
Col1a1-K18-hACE2
K18-hACE2

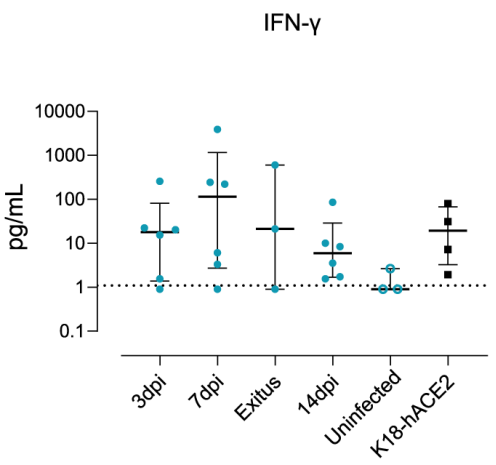

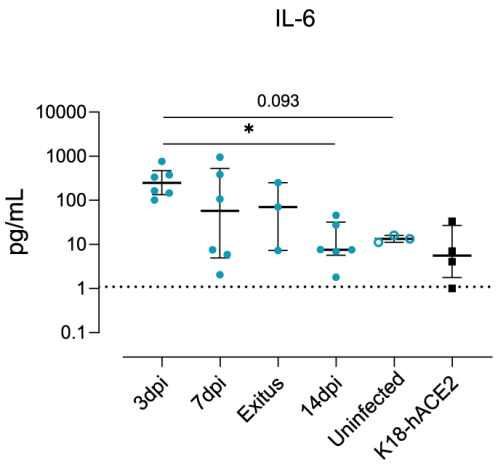

Col1a1-K18-hACE2 Infected
Col1a1-K18-hACE2 Uninfected
K18-hACE2 Infected

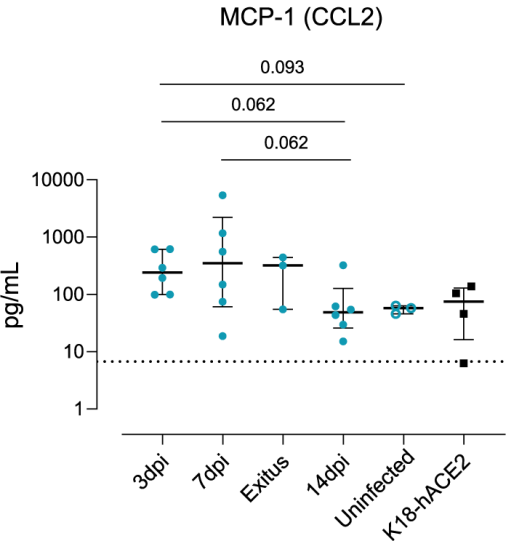

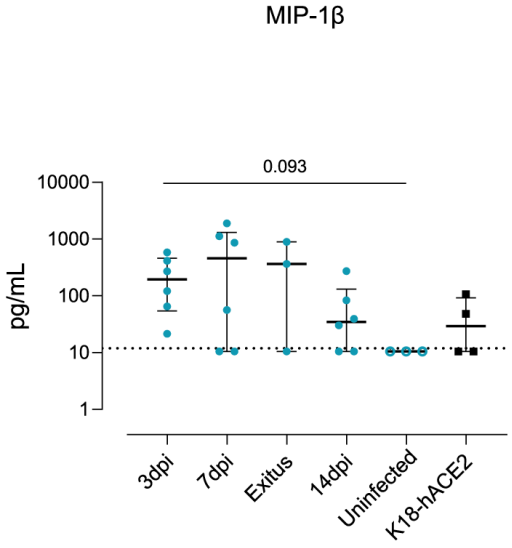

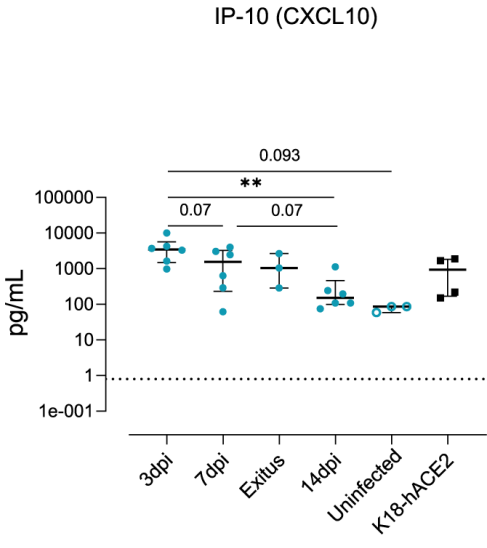

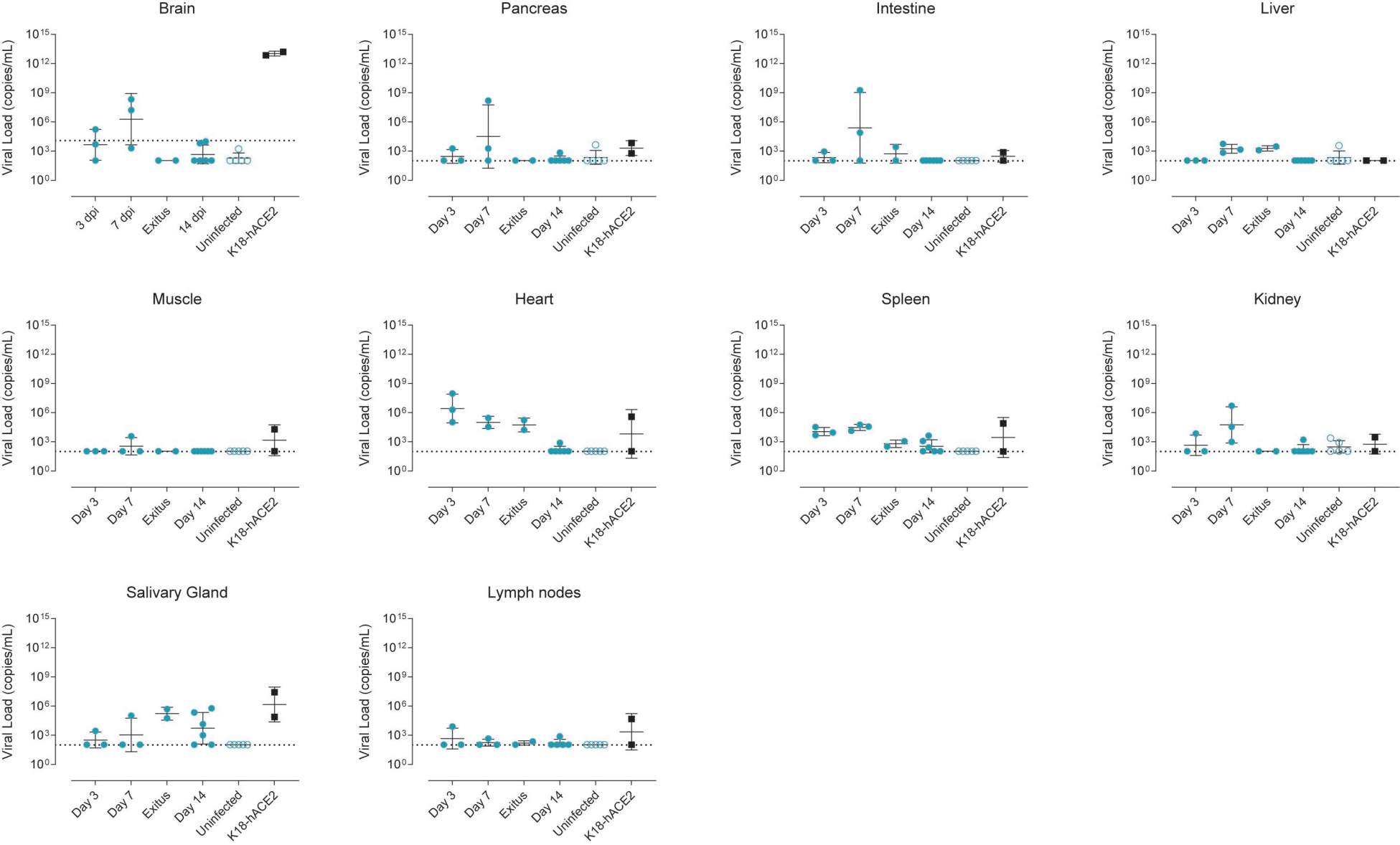
Brain
Pancreas
Intestine
Liver
Muscle
Heart
Spleen
Kidney
Salivary Gland
Lymph nodes
Viral Load (copies/mL)
10^{15}
10^{12}
10^{9}
10^{6}
10^{3}
10^{0}
3 dpi
7 dpi
Day 3
Day 7
Exitus
Day 14
Uninfected
K18-hACE2

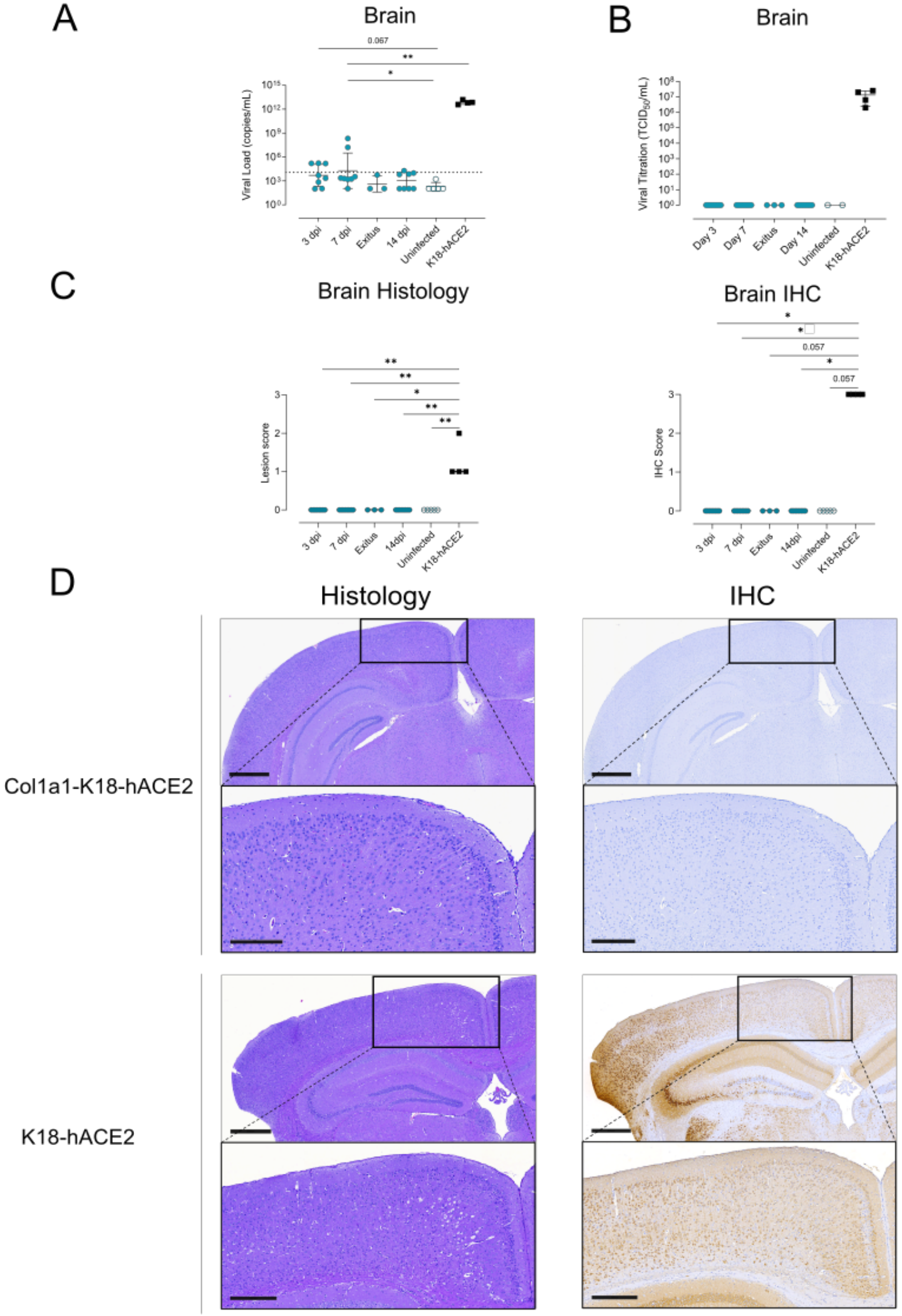
A
Brain
0.067
**
*
Viral Load (copies/mL)
3 dpi
7 dpi
Exitus
14 dpi
Uninfected
K18-hACE2
B
Brain
Viral Titration (TCID50/mL)
Day 3
Day 7
Exitus
Day 14
Uninfected
K18-hACE2
C
Brain Histology
Lesion score
3 dpi
7 dpi
Exitus
14dpi
Uninfected
K18-hACE2
Brain IHC
IHC Score
0.057
D
Histology
IHC
Col1a1-K18-hACE2
K18-hACE2